Identifying deep moonquake nests using machine learning model on single lunar station on the far side of the Moon

Josipa Majstorović[1], Philippe Lognonné[2], Taichi Kawamura[3], and Mark Paul Panning[4]

[1]Institut de Physique du Globe de Paris
[2]Université Paris Cité, Institute de physique de globe de Paris, CNRS
[3]Université Paris Cité, Institut de physique du globe de Paris, CNRS
[4]Jet Propulsion Laboratory, California Institute of Technology

December 8, 2023

Abstract

One of the future NASA space program includes the Farside Seismic Suite (FSS) payload, a single station with two seismometers, on the far side of the Moon. During FSS operations, the processing of the data will provide us with new insight into the Moon's seismic activity. One of Apollo mission finding is the existence of deep moonquakes (DMQ), and the nature of their temporal occurrence patterns as well as the spatially clustering. It has been shown that DMQs reside in about 300 source regions. In this paper we tackle how we can associate new events with these source regions using the single station data. We propose a machine learning model that is trained to differentiate between DMQ nests using only the lunar orbital parameters related to DMQ time occurrences. We show that ML models perform well (with an accuracy >70%) when they are trained to classify less than 4 nests.

Identifying deep moonquake nests using machine learning model on single lunar station on the far side of the Moon

Josipa Majstorović[1], Philippe Lognonné[1], Taichi Kawamura[1], Mark P. Panning[2]

[1]Université Paris Cité, Institut de physique du globe de Paris, CNRS, Paris, France
[2]Jet Propulsion Laboratory, California Institute of Technology, Pasadena, CA, USA

Key Points:

- As a part of the future space mission NASA will deploy a new seismic station to Schrödinger Basin on the far side of the Moon.
- We propose a machine learning model trained to classify deep moonquakes using the lunar orbital parameter.
- The models perform with accuracy greater than 70% when trained to classify combinations of four or fewer nests.

Corresponding author: Josipa Majstorović, josipa.majstorovic@protonmail.com

Abstract

One of the future NASA space program includes the Farside Seismic Suite (FSS) payload, a single station with two seismometers, on the far side of the Moon. During FSS operations, the processing of the data will provide us with new insight into the Moon's seismic activity. One of Apollo mission finding is the existence of deep moonquakes (DMQ), and the nature of their temporal occurrence patterns as well as the spatially clustering. It has been shown that DMQs reside in about 300 source regions. In this paper we tackle how we can associate new events with these source regions using the single station data. We propose a machine learning model that is trained to differentiate between DMQ nests using only the lunar orbital parameters related to DMQ time occurrences. We show that ML models perform well (with an accuracy $> 70\%$) when they are trained to classify less than 4 nests.

Plain Language Summary

The future space missions will provide us with various new lunar data, one of which will be ground vibration measurement. The studies of these measurements from the Apollo era in 70s, showed that Moon can host various events. The most intriguing ones are deep moonquakes (DMQs), which are events associated with the displacement deep within the lunar interior. It has been shown that DMQs occur in the specific locations, which are called nests, and that their temporal occurrence is related to the monthly motion of the Moon around the Earth. In this paper we tackle how we can associate new events from only one station located on the far side of the Moon with these known locations of DMQs. We propose a machine learning model that is trained to classify DMQ nests, only using the information about their temporal occurrences, e.g. time of the event, described in terms of different lunar events. We report that models are performing well (with an accuracy $> 70\%$) when they are trained to classify 4 or fewer nests. This gives us a good first approximation about the nest identification.

1 Introduction

We are at the beginning of a golden age of lunar exploration as many nations, together with private companies, are establishing numerous efforts to obtain new scientific measurement of the Moon (Weber et al., 2021; Pickrell, 2022; Kawamura et al., 2022). In light of this, NASA established the Artemis program which should land a crewed mission at the lunar south pole (Witze, 2022). This would be the first attempt of a crewed landing after the successful Apollo missions in 1970's. Before Artemis missions land on the Moon, NASA has also established the Commercial Lunar Payload Services (CLPS) program to land scientific payloads on the Moon using commercial landers. The Farside Seismic Suite (FSS) is one of the selected payloads, and it will deliver two seismometers to Schrödinger Basin on the far side of the Moon (Panning et al., 2021; Standley et al., 2023; Cutler et al., 2023): one vertical Very BroadBand seismometer, and Short Period sensor, both spare or derived from the SEIS experiment sensors (Lognonné et al., 2019, 2020) from the InSight mission to Mars (Banerdt et al., 2020).

The Apollo missions showed the importance of deploying sensors on the surface of the Moon, since a great deal of our knowledge about the Moon comes from the analysis of data acquired during the Apollo era (Lognonné & Johnson, 2015). Thus, analyzing ground motion measurements provided the community with the first constraints on the lunar interior and the activity at the surface (Nakamura et al., 1982a, 1982b; Khan et al., 2000; Khan & Mosegaard, 2002; Khan et al., 2014; Lognonné et al., 2003; Gagnepain-Beyneix et al., 2006; Weber et al., 2010; Garcia et al., 2011; Kawamura et al., 2017; Garcia et al., 2019; Nunn et al., 2020). It has also revealed that the Moon can host events of various origins, such as shallow and deep moonquakes, meteoroid and artificial impacts (Toksöz et al., 1974; Dainty et al., 1975; Lammlein, 1977a; Nakamura, 1983, 2003, 2005).

Today, we have more than twelve thousands events, out of which the deep moonquakes (DMQs) form the most numerous group (Nakamura et al., 1981; Nakamura, 2005).

DMQs are a distinctive group of seismic events that originate from depths between 700 and 1200 km, at high pressure and temperature conditions, where little brittle deformation is expected. Due to very high waveform similarity between quakes, the DMQs have been clustered into about 300 source regions or nests (Nakamura, 2003). This has interpreted to be a consequence of DMQs occurring repeatedly at the fixed nests, which are located mostly on the near side of the Moon. It has been shown that time occurrence of the DMQs is correlated with the monthly motion of the Moon around the Earth. Thus, DMQ occurrences exhibit tidal periodicities and furthermore, the associated high strain rates might explain brittle processes (Kawamura et al., 2017). However, the real causes of their origins are yet to be discovered. There are two puzzling fact about their origin: a) cyclic tidal stresses, caused by the monthly motion of Moon around Earth, are far less than the estimated confining pressures where DMQs occurs (Cheng & Toksöz, 1978; Minshull & Goulty, 1988a); b) do we need both, tectonic and ambient tidal stresses, to explain their mechanical origin (Frohlich & Nakamura, 2009).

To better constrain the lunar interior and unravel the cause of DMQs, it is important to locate new events and associate them with the known nest locations from Apollo with future lunar missions like FSS. These new observations will add, for each new nest, a new differential $t_s - t_p$ measurement constraining the deep interior with a different epicentral distance. However, due to the mission requirements, it is extremely likely that, at the beginning, we might have only one lunar station at the disposal. Therefore, in this paper we study the problem of DMQ nest identification without using waveform information. This is due to the new location of the recording station, which will not match existing Apollo-era waveform templates due to different propagation paths. We propose a machine learning (ML) model that is trained to identify nests within the set of nests of similar differential travel times. The main features used for the model training are related to the fact that different nests respond differently to lunar cycle.

Very early studies have shown correlation between lunar transient events and position of the Moon related to the Earth (Middlehurst, 1967; Cameron & Gilheany, 1967; Moore, 1968). This further encouraged observations that some moonquakes occur with periods that reflect Earth-Moon-Sun relationship (Ewing et al., 1971). Later, it has been shown that the occurrence of DMQs are related to tidal stress cycles, and correlations between DMQs occurrence times and lunar monthly tidal cycles have been indicated (Lammlein et al., 1974; Toksöz et al., 1977; Lammlein, 1977b; Cheng & Toksöz, 1978; Minshull & Goulty, 1988b). The lunar cycle can be explained with three lunar months: synodic, draconic, anomalistic. Synodic month is the period of lunar phases such as New Moon, First Quarter, Full Moon, Last Quarter. Draconic month is the period between two nodes, ascending or descending, where the nodes are points at which the Moon's orbit plane crosses the ecliptic plane towards which it is inclined of about 5.14°. Anomalistic month is the period between two extreme points, perigee and apogee, since the Moon's orbit approximates an ellipse rather than a circle. Earlier studies counted the number of events per day as a function of time and found 0.5 and 1 month signals in the occurrence times related to anomalistic and draconic period of 27 days (Lammlein et al., 1974; Lammlein, 1977b). The same studies also indicated 206-day and 6-year periods, related to the Sun's perturbation on the lunar orbit and the relative precession of the perigee of the Moon's orbit. Subsequently, many recent papers studied and confirmed tidal periodicities of DMQs and more (Bulow et al., 2005, 2007; Bills et al., 2008; Frohlich & Nakamura, 2009; Weber et al., 2009, 2010; Turner et al., 2022).

Based on the previous papers, it is clear that DMQ nests exhibit some clear temporal patterns in their occurrences, and that these are correlated with Moon-Earth system. Therefore, the open question is whether we can design features which would reflect these temporal patterns and to further use those features to study the nest identifica-

tion with one lunar station. In this paper we tackle the question of defining optimal features and the machine learning model. The paper is organised as follows: first, we discuss data used in the analysis, the existing catalog of DMQ events. Second, we discuss the feature design. Third, we introduce a machine learning model. Fourth, we discuss successes and pitfalls of the machine learning model for nest identification applied to different combination of nests. We conclude how this study can offer some first estimates of the nest location in the future lunar missions.

2 Data

We start with the existing catalog of lunar events (Nakamura et al., 1981), which was updated in 2008 and modified in 2018 (Nunn et al., 2020). Catalog contains a list of events (shallow and deep moonquakes, meteoroid and artificial impacts) with attributes such as date and time of the event occurrence, signal envelope amplitude as measured in mm on a standard plot, data availability per station, and the nest (source) classification for DMQs. It is important to note that the source classification is not an exact location defined by latitude and longitude, rather a result from the waveform cross-correlation and single-link cluster analysis (Nakamura, 2003). This analysis positively clustered around 7k DMQs into 77 nests, where the largest nest is associated with label A1. This nest contains 443 quakes and it is placed on the near side of the Moon.

2.1 Catalog processing: nest sets based on travel time information

Earlier studies published lunar interior models and location of DMQ nests in terms of latitude and longitude by picking P and S travel times on the quake waveforms (Garcia et al., 2019, review of these picks). Using lunar interior models and nest locations we can define nests that are close by in distance if we consider only the t_{sp} travel time measurements. To do so we assume that a) our single lunar station is located on the far side in Schrödinger Basin (FSS landing site at 71.378°S, 138.248°E), b) nests' latitudes and longitudes from (Lognonné et al., 2003), c) calculated P- and S- wave travel times (t_p and t_s, respectively) using lunar velocity model between landing site and locations of DMQ nests. By having t_s and t_p we can calculate $t_{sp} = t_s - t_p$ for all nests and models shown in Figure 1 (see Text S1 and Figure S1 for further explanation). Next, we count for each nest how many there are with the similar t_{sp} travel time measurement assuming a picking error of 5 seconds as shown in Figure 1A, consistent with the average picking error in Lognonné et al. (2003). This count provides us with the different sets S_i, shown in Figure 1A, that contain nests N_j of similar travel times. In other words, if we are able to measure t_s and t_p of the new lunar event with accuracy within 5 seconds, we are not able to differentiate between nests that belong to different sets S_i. Therefore, to further tackle the nest identification problem we proceed to associate each event with a combination of lunar orbital measurements.

2.2 Feature selection based on the lunar orbital information

It has been shown that the DMQ temporal patterns in time occurrences are related to different lunar cycles and that these patterns differ from nest to nest. Three lunar cycles are synodic, draconic, anomalistic, and they all have similar periods, but are marked by different motions, either as the motion between two Full Moons phases, or two nodes, or two apsis, respectively. One can list all the events when Moon is in the Full Moon (New Moon) phase, passing through ascending (descending) node or perigee (apogee) by simply looking at the Moon's ephemeris (Meeus, 1991). To make sure that we take into account the temporal patterns, we design the main three features as a time difference between the time of the quake in the nest and the time of the Moon's Full Moon, ascending node and perigee, denoting it as $\Delta t_{FullMoon}, \Delta t_{AscendingNode}, \Delta t_{Perigee}$, respectively. We can achieve the same effect by taking the other three time axis as referent one (New

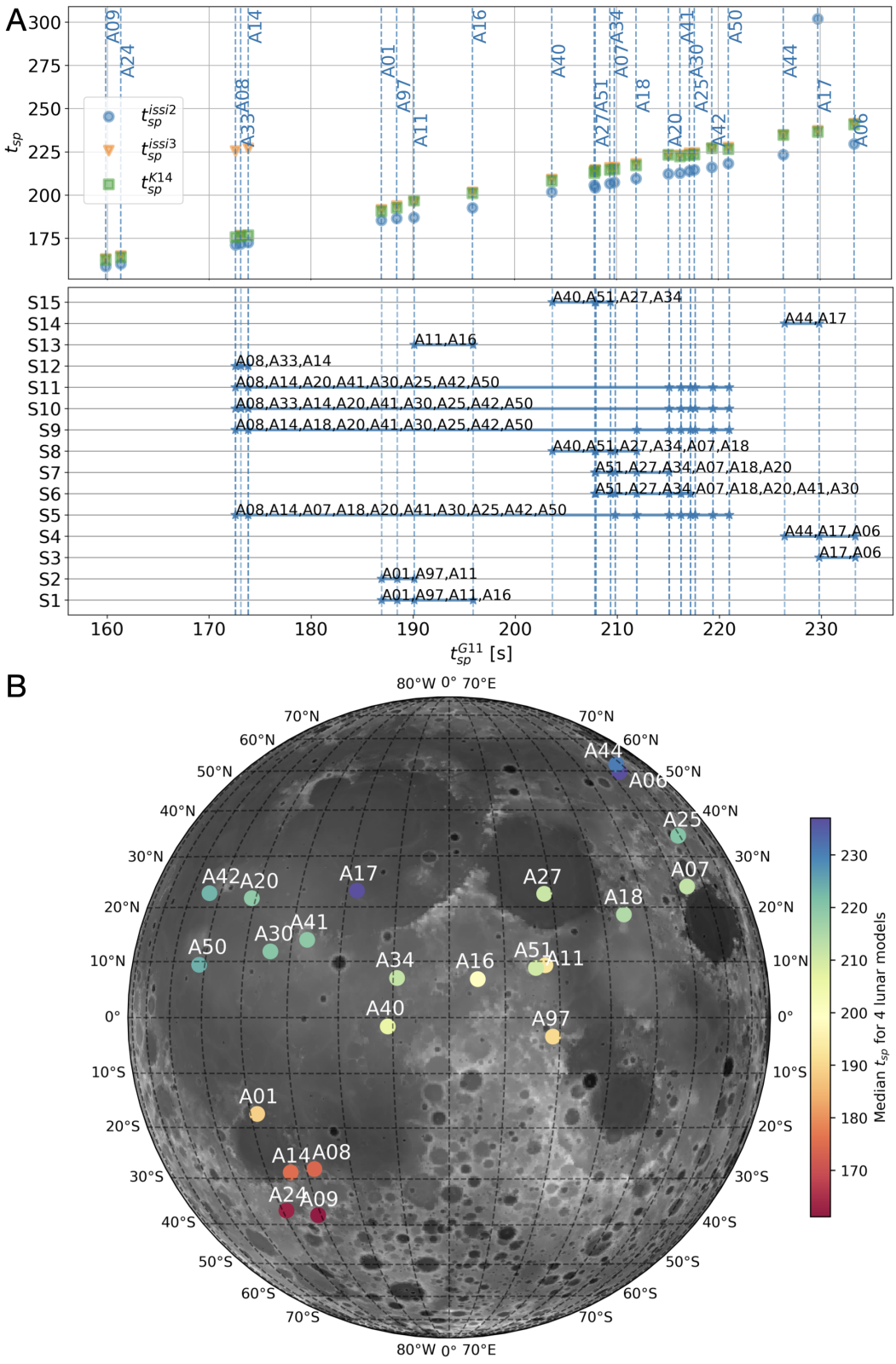

Figure 1. Location study of the DMQ nests from the perspective of $t_{sp} = t_s - t_p$ travel time measurements if we place station in the Schrödinger Basin and consider four different lunar models. A) Upper panel: t_{sp} travel time measurements for four lunar models from Garcia et al. (2011) (G11), Garcia et al. (2019) (issi2, issi3), (Khan et al., 2014) (K14) with nest labels; A) Lower panel: Sets S_i which represent nests with similar travel times if we consider a travel time error of 5 seconds. B) Lunar map with the nests locations where the color indicate the median t_{sp} for four lunar model.

Moon, descending node, and apogee). The next feature is related to the Moon position within its orbit as in Frohlich and Nakamura (2009). The angle between the direction of perigee and the current position of the body, as seen from the main focus of the ellipse, is called the true anomaly, denoted further as γ. Further, as one of the feature we also use the interval time between two quakes in the nest, noted as $e_{i+1} - ei$, as in Weber et al. (2010). And the last two features are related to the position of the Moon with respect to the Earth, and these are the distance, d, itself and the rate of the distance change, $\dot{d}$, as in Bills et al. (2008).

The selected features all have different ranges and we refer to them as raw data. To train a model that is able to generalise well for a given problem sometimes it is necessary to transform raw data to a form that is more suitable for training (Langer et al., 2019). By applying transformation on the raw data we may obtain a mapping which better reveals patterns in our data. Therefore, we chose to apply trigonometric transformation of the true anomaly angle γ, to properly address the jump discontinuities in the feature when angle goes from 2π to 0, due to it's cyclic nature. This is addressed by transforming true anomaly angle γ to pair of $[\cos\gamma, \sin\gamma]$. An example of all eight features are shown in Figure S2 for nest A1.

3 Methodology

When new lunar data arrives, we shall be able to differentiate events in groups based on the waveform similarity measurement. And we shall be able to measure their P and S travel times, and thus form set of nests from Section 2.1. Final step would be to associate these new events with the existing Apollo nests if possible. This nest identification from a single lunar station is a supervised classification problem. The model is trained in a predictive way by taking into account nest locations as labels and nest lunar orbital parameters as input data. Since we want to predict a class (nest), but we do not have statistically large data set (as previously mentioned A1 has 443 quakes), we choose to train a Random Forest (RF) Classifier, since RF can perform well with any size of datasets and tend not to overfit (Ho, 1995; Breiman, 2001).

Random Forest (RF) is a machine learning technique that is based on decision trees (Breiman et al., 1984; Quinlan, 1986) and bootstrap aggregating (Breiman, 1996), where the main output is reached by majority votes among an ensemble of randomised decision trees. A main building unit, a decision tree, is a tree-like learning algorithm where each internal node tests on attribute, each branch corresponds to attribute value and each leaf node represents the final prediction. Usually, during the training phase thresholds, order and number of inequality operations within internal nodes are learned. The hyperparameters that define a RF structure, such as the number of trees, and measure which maximises diversity between classes, are determined beforehand (see Text S2 and Figure S3).

RF also provides an assessment of the feature or input variable importance which might give us an insight of how the model reached its prediction. To assess the feature importance, the RF removes one of the features while it keeps the rest constant, and it measures, among others, the accuracy decrease (Breiman, 2001). RF models are able to solve regression and classification problems, as well as two- and multi-class problems. It has been show that RF can perform with high accuracy even though there are only a few parameters to tune.

In our case, during the training phase, the RF model has access to the extracted features of the individual quakes and the nest labels. The training is performed on a subset of the data, while the model performance is evaluated on the test subset, which the model has never seen. Evaluation is accomplished by comparing the model's predicted class (nest) with the ground truth one. The statistical performance of the model is pre-

sented with confusion matrix and Receiver Operating Characteristic (ROC) curve. We expect that in the case of the ideal RF Classifer the diagonal of the confusion matrix is equal to 1 (and off-diagonal elements are zero), while ROC curve is passing through the left upper corner.

4 Results and discussion

4.1 Training and testing on two largest nests

We first test the hypothesis whether it is possible to differentiate two DMQ nests using the lunar orbital parameters (features). For this, we select the two largest nests, A1 and A8, with a total size of 768 events and ratio A1:A8=$0.57 : 0.43$ (see feature distributions in Figure S4).

Training and testing our base RF model (see Text S2) with the normalised and not normalised input data, we end up selecting to work with the normalised input data since this model performed better (see Figure S5 and S6). The base model trained with the normalised input data performed with an accuracy of 89%, while precision, recall and f1-score for the A1 nest is 88%, 94%, 91%, respectively, and for A8 is 90%, 80%, 85%, respectively (see Figure S6B) with only the occurrence time knowledge. The ROC curve is above the random classifier curve, meaning that the base model is not randomly classifying A1 and A8 nests (see Figure S6C). Out of eight features, the first five most important are $cos(\gamma)$, $\Delta t_{Perigee}$, d, $\Delta t_{AscendingNode}$, $e_{i+1} - e_i$ (see Figure S6D). We notice that $cos(\gamma)$ is the feature with the most important contribution to the model learning. This might be because A1 and A8 have reversed distributions for $cos(\gamma)$ feature (see Figure S 4D).

We proceed into testing learning robustness of our base model in a series of experiments (see Text S2 and Figures S7-S12), all of which indicate that the model is stable. This implies that the base model generalizes well, and not over fit the results. Further, if we examine why the base model sometimes mislabels the nests (Figure S13), we notice that the 2D manifold (see Text S3) of feature space spanned by the input data, calculated by t-sne method (van der Maaten & Hinton, 2008), is not perfectly separated. It seems this segregation might be dominated by a single feature, and that is $\Delta t_{AscendingNode}$ (see Figure S14 and S15A).

4.2 Training and testing on three and more nests

In this section we study how the performance of our base RF model from Section 4.1 changes by adding more nests. We carry out three tests for the next combinations and their ratios: A1-A8-A18 (45%-33%-22%), A1-A8-A18-A6 (38%-28%-18%-15%), A1-A8-A18-A6-A14 (33%-25%-16%-13%-12%), where the three added nests are the three largest nests besides A1 and A8.

The analysis shows that by adding more nests, the performance of our base model deteriorates since the accuracy drops from 88% to 59% (see Figures S16-S19). By adding a 3rd nest, and we notice that A1 and A8 recalls deteriorate slightly, and 50% is A18 events are classified either as A1 or A8 (see Figure S16). Yet, the precision of A18 is the highest. Features, $e_{i+1}-e_i$ and $\dot{d}$, gain importance. Yet, the importance of all features become more equalized. By adding a 4th nest, A6, the recall of A1 nest improves, recall of A8 nest deteriorates even more than before, recall of A18 improves notably, and the new added nest A6 has a recall of 46%, by having most of its events misclassified only as A1 nest, and not a single event as A18 (see Figure S17). This might implies that A18 and A6 nests have completely different source mechanisms. Less notably than before, the importance of all features is becoming more equalized. Lastly, by adding a 5th nest, A14, the recall of A1 and A8 become the highest, and three other nests perform with

recall less than 50%, and their most mislabelled data points are associated with A1 nest (see Figure S18). The importance between features is almost equalized, yet the interval time $e_{i+1} - e_i$ is the only feature that stands out.

These results might imply that by adding more nests, we add more complexity into the problem, since we might be adding nests that have similar source mechanisms. Having similar source mechanisms means that sources are triggered by tides is the same way, so their lunar orbital features have similar characteristics, and we cannot differentiate between nests without having more data. Furthermore, it seems that the only significantly important feature is the interval time, the only feature that does not reflect the lunar orbital information.

Checking the two dimensional representation of the feature space constructed by the feature combination of nests A1-A8-A18-A6-A14, we might conclude that for this particular set it is to some degree impossible to completely differentiate between nests due to the lack of data (see Figure S20).

4.3 Training and testing on nest sets

Using the same base RF model from Section 4.1, we proceed to train and test how well we can differentiate nests that belong to the same set shown in Figure 1. We analyze them in three separate groups by the frequency of the nest they contain: A) S1, S2, S3, S4, S12, S13, S14, S15; B) S5, S6, S7, S8; C) S9, S10, S11. The results are shown in Figure 2A, B, and C, respectively.

We observe high value of recall for most of the nests, as well as high accuracy for most of the sets (see Figure 2). Sets that have $<= 4$ nests perform better than those with more nests, as in sets from group A shown in Figure 2B. When the nest's recall is very low or zero (A11, A30, A41, A42, A50), it signifies a nest with very few events (see ratio of nests in all sets in Figure S18). If we take an example of nest A20, we notice that it has constant recall in many sets (see Figure 2B and C), even though it is not the biggest nest in the set (see Figure S21). Thus, not only the size but probably also the uniqueness of the features determine the success of identifying the nest.

The importance of different features is shown in Figure 3 for all three groups. On one hand, removing just one nest could change the feature importance, as in the case of S2 (where we remove A16) versus S1. On the other hand, we notice that the feature importance does not drastically change when comparing results for sets S3 and S4, where we add nest A44, even though the nest itself is large in size (see Figure S21). For the sets in group B, the feature importance is stable with respect to adding or removing nests. It is quite similar for group C, where only one set S8 has different feature importance. We notice that sets which contain $<= 4$ nests (as in group A), there is usually one or two important features, while for sets with > 4 nests there is equalisation of the feature importance (as in groups B and C). This might imply that a single lunar orbital parameter is enough to explain the occurrence of the nests, which are unique in nature. Mixing more nests suggests that we might be mixing nests with similar temporal patterns, thus learning how to differentiate them is more challenging. Moreover, the feature importance changes for sets that have unique combinations of nests, which may hint that these nests have different source mechanisms.

If we consider a 2D manifold spanned by the sets from groups A, B, C (see Figures S22, S23, S24, respectively), we notice that unique segregation in this space correlates with the RF model accuracy. Nests that form closely spaced homogenized clusters in the 2D manifold tend to be correlated with models that scored high recall for these nests.

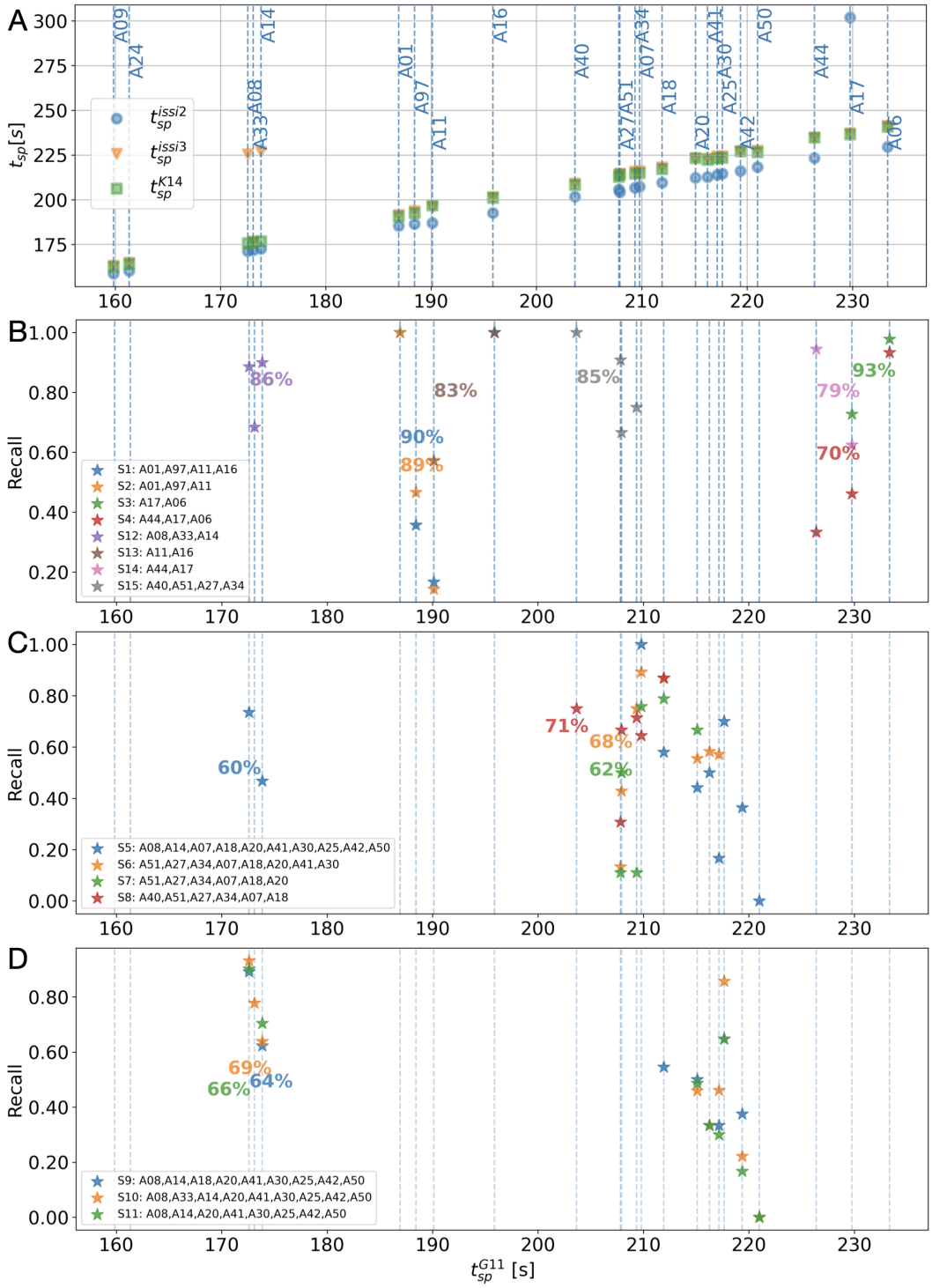

Figure 2. Performance of RF models designed to classify nests within different sets. A) Travel times t_{sp} for four lunar model from Garcia et al. (2011) (G11), Garcia et al. (2019) (issi2, issi3), (Khan et al., 2014) (K14) with nest labels. B) Recall for individual nests within each set with respect to their travel times labeled with sets to which they belong and the scored accuracy of this set. C) and D) same as B) just for different group of sets.

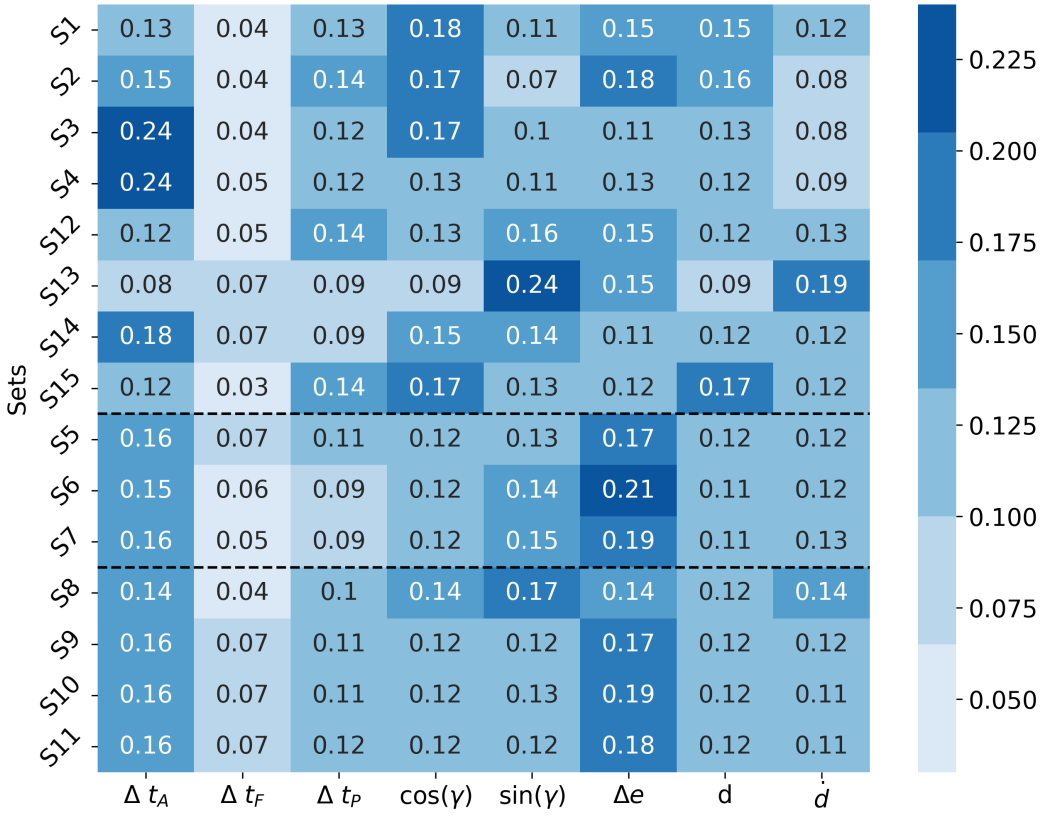

Figure 3. Feature importance for Random Forest models associated with different travel time sets shown in Figure 1.

5 Conclusion

In this paper we propose how to tackle DMQ nest identification during future lunar missions that will likely host only one station on the far side of the Moon. We propose constraining their location by using differential time travel measurement t_{sp} and parameters related to the temporal patterns of the DMQ occurrence. First, in our analysis we assume that we cannot differentiate between nests whose differences in travel time are less than 5 seconds. Thus, we form set of nests that have similar travel times. Second, for each event within the nests we calculate features that are used to build a Random Forest model. This model is trained to differentiate between distinct nests. The features used for training are build by associating each event in all nests with the time difference between events' origin time and time of lunar ascending node, Full Moon phase, perigee, then position of the Moon in its orbit expressed by true anomaly angle, distance of the Moon from the Earth, rate change of this distance, and the time between two successive quakes. We show that by training Random Forest models to differentiate between distinct nests within sets, we can obtain models with high accuracy (more than half of the models score above 70% accuracy). Yet, the performances of these models depend on the number of nests within the set. More nests implies that the problem is more difficult to solve, probably because a) nests might have similar source mechanisms, b) the number of events within nests is unbalanced, and c) we don't have enough data. Since RF models also arrange features by their importance to make a final classification decision, we observe that the importance of the features change with different sets. This complements the findings of previous papers, since it signifies that nests do correspond to different lunar events, which eventually might be connected to the distribution of tidal stresses during these events. Finally, our model provides a good first approximation of the nest identification. And as the catalog of new events grows, it will be straightforward to retrain RF model with the new enlarged dataset.

Open Research Section

The deep moonquake catalog used in this study is published in Nakamura et al. (1981), and revisited in Nunn et al. (2020). Python package Skyfield used to calculate Moon's orbital parameters based on JPL ephemeris can be found on the website `https://rhodesmill.org/skyfield/` (Rhodes, 2019, Software). For our implementation of the Random Forest algorithm we use Scikit-learn machine learning Python library (Pedregosa et al., 2011).

Acknowledgments

French co-authors thanks the French Space Agency, CNES, for supporting this research in the frame of the French contribution to FSS as well as IDEX Paris Cité (ANR-18-IDEX-0001). MPP was supported by funds from the Jet Propulsion Laboratory, under contract with the National Aeronautics and Space Administration (NASA).

References

Banerdt, W. B., Smrekar, S. E., Banfield, D., Giardini, D., Golombek, M., Johnson, C. L., ... others (2020). Initial results from the insight mission on mars. *Nature Geoscience*, *13*(3), 183–189.

Bills, B. G., Bulow, R., & Johnson, C. L. (2008). Influence of earth-moon orbit geometry on deep moonquake occurrence times. *Lunar Planet. Sci., XXXIX*.

Breiman, L. (1996). Bagging predictors. *Machine learning*, *24*, 123–140.

Breiman, L. (2001). Random forests. *Machine learning*, *45*, 5–32.

Breiman, L., Friedman, J., Stone, C. J., & Olshen, R. A. (1984). *Classification and regression trees*. CRC press.

Bulow, R., Johnson, C., Bills, B., & Shearer, P. (2007). Temporal and spatial properties of some deep moonquake clusters. *Journal of Geophysical Research: Planets*, *112*(E9).

Bulow, R., Johnson, C., & Shearer, P. (2005). New events discovered in the apollo lunar seismic data. *Journal of Geophysical Research: Planets*, *110*(E10).

Cameron, W. S., & Gilheany, J. J. (1967). Operation moon blink and report of observations of lunar transient phenomena. *Icarus*, *7*(1-3), 29–41.

Cheng, C. H., & Toksöz, M. N. (1978). Tidal stresses in the moon. *Journal of Geophysical Research: Solid Earth*, *83*(B2), 845-853. Retrieved from `https://agupubs.onlinelibrary.wiley.com/doi/abs/10.1029/JB083iB02p00845` doi: https://doi.org/10.1029/JB083iB02p00845

Cutler, J. W., Nguyen, T. A., Kano, T., Kumar, Y. R. L., Panning, M., April, S., & Haque, S. (2023). Overview of the avionics design for the farside seismic suite. In *Aiaa scitech 2023 forum.* Retrieved from `https://arc.aiaa.org/doi/abs/10.2514/6.2023-1880` doi: 10.2514/6.2023-1880

Dainty, A., Goins, N., & Toksoz, M. (1975). Natural lunar seismic events and the structure of the moon. In *In: Lunar science conference, 6th, houston, tex., march 17-21, 1975, proceedings. volume 3.(a78-46741 21-91) new york, pergamon press, inc., 1975, p. 2887-2897.* (Vol. 6, pp. 2887–2897).

Ewing, M., Latham, G., Press, F., Sutton, G., Dorman, J., Nakamura, Y., ... Kovach, R. (1971). Seismology of the moon and implications on internal structure, origin and evolution. *Highlights of astronomy*, *2*, 155–172.

Frohlich, C., & Nakamura, Y. (2009). The physical mechanisms of deep moonquakes and intermediate-depth earthquakes: How similar and how different? *Physics of the Earth and Planetary Interiors*, *173*(3), 365-374. Retrieved from `https://www.sciencedirect.com/science/article/pii/S0031920109000338` doi: https://doi.org/10.1016/j.pepi.2009.02.004

Gagnepain-Beyneix, J., Lognonné, P., Chenet, H., Lombardi, D., & Spohn, T. (2006). A seismic model of the lunar mantle and constraints on temperature and mineralogy. *Physics of the Earth and Planetary Interiors*, *159*(3-4), 140–166.

Garcia, R. F., Gagnepain-Beyneix, J., Chevrot, S., & Lognonné, P. (2011). Very preliminary reference moon model. *Physics of the Earth and Planetary Interiors*, *188*(1-2), 96–113.

Garcia, R. F., Khan, A., Drilleau, M., Margerin, L., Kawamura, T., Sun, D., ... others (2019). Lunar seismology: An update on interior structure models. *Space Science Reviews*, *215*, 1–47.

Ho, T. K. (1995). Random decision forests. In *Proceedings of 3rd international conference on document analysis and recognition* (Vol. 1, pp. 278–282).

Kawamura, T., Grott, M., Garcia, R., Wieczorek, M., de Raucourt, S., Lognonné, P., ... others (2022). An autonomous lunar geophysical experiment package (algep) for future space missions: In response to call for white papers for the voyage 2050 long-term plan in the esa science program. *Experimental Astronomy*, *54*(2-3), 617–640.

Kawamura, T., Lognonné, P., Nishikawa, Y., & Tanaka, S. (2017). Evaluation of deep moonquake source parameters: Implication for fault characteristics and thermal state. *Journal of Geophysical Research: Planets*, *122*(7), 1487–1504.

Khan, A., Connolly, J. A. D., Pommier, A., & Noir, J. (2014). Geophysical evidence for melt in the deep lunar interior and implications for lunar evolution. *Journal of Geophysical Research: Planets*, *119*(10), 2197-2221. Retrieved from `https://agupubs.onlinelibrary.wiley.com/doi/abs/10.1002/2014JE004661` doi: https://doi.org/10.1002/2014JE004661

Khan, A., & Mosegaard, K. (2002). An inquiry into the lunar interior: A nonlinear inversion of the apollo lunar seismic data. *Journal of Geophysical Research: Planets*, *107*(E6), 3–1.

Khan, A., Mosegaard, K., & Rasmussen, K. L. (2000). A new seismic velocity model for the moon from a monte carlo inversion of the apollo lunar seismic data. *Geophysical Research Letters*, *27*(11), 1591–1594.

Lammlein, D. R. (1977a). Lunar seismicity and tectonics. *Physics of the Earth and Planetary Interiors*, *14*(3), 224-273. Retrieved from https://www.sciencedirect.com/science/article/pii/0031920177901753 doi: https://doi.org/10.1016/0031-9201(77)90175-3

Lammlein, D. R. (1977b). Lunar seismicity and tectonics. *Physics of the Earth and Planetary Interiors*, *14*(3), 224–273.

Lammlein, D. R., Latham, G. V., Dorman, J., Nakamura, Y., & Ewing, M. (1974). Lunar seismicity, structure, and tectonics. *Reviews of Geophysics*, *12*(1), 1–21.

Langer, H., Falsaperla, S., & Hammer, C. (2019). *Advantages and pitfalls of pattern recognition: selected cases in geophysics*. Elsevier.

Lognonné, P., Banerdt, W. B., Giardini, D., Pike, W. T., Christensen, U., Laudet, P., ... others (2019). Seis: Insight's seismic experiment for internal structure of mars. *Space Science Reviews*, *215*, 1–170.

Lognonné, P., Banerdt, W. B., Pike, W. T., Giardini, D., Christensen, U., Garcia, R. F., ... others (2020). Constraints on the shallow elastic and anelastic structure of mars from insight seismic data. *Nature Geoscience*, *13*(3), 213–220.

Lognonné, P., Gagnepain-Beyneix, J., & Chenet, H. (2003). A new seismic model of the moon: implications for structure, thermal evolution and formation of the moon. *Earth and Planetary Science Letters*, *211*(1-2), 27–44.

Lognonné, P., & Johnson, C. (2015). 10.03—planetary seismology. *Treatise on geophysics*, *2*, 65–120.

Meeus, J. (1991). Astronomical algorithms. *Richmond*.

Middlehurst, B. M. (1967). An analysis of lunar events. *Reviews of Geophysics*, *5*(2), 173–189.

Minshull, T., & Goulty, N. (1988a). The influence of tidal stresses on deep moonquake activity. *Physics of the Earth and Planetary Interiors*, *52*(1), 41-55. Retrieved from https://www.sciencedirect.com/science/article/pii/0031920188900568 doi: https://doi.org/10.1016/0031-9201(88)90056-8

Minshull, T., & Goulty, N. (1988b). The influence of tidal stresses on deep moonquake activity. *Physics of the earth and planetary interiors*, *52*(1-2), 41–55.

Moore, P. (1968). Transient lunar phenomena: A review, 1967. *J. Br. Astron. Assoc.*, *78*, 138–144.

Nakamura, Y. (1983). Seismic velocity structure of the lunar mantle. *Journal of Geophysical Research: Solid Earth*, *88*(B1), 677-686. Retrieved from https://agupubs.onlinelibrary.wiley.com/doi/abs/10.1029/JB088iB01p00677 doi: https://doi.org/10.1029/JB088iB01p00677

Nakamura, Y. (2003). New identification of deep moonquakes in the apollo lunar seismic data. *Physics of the Earth and Planetary Interiors*, *139*(3), 197-205. Retrieved from https://www.sciencedirect.com/science/article/pii/S0031920103002103 doi: https://doi.org/10.1016/j.pepi.2003.07.017

Nakamura, Y. (2005). Farside deep moonquakes and deep interior of the moon. *Journal of Geophysical Research: Planets*, *110*(E1). Retrieved from https://agupubs.onlinelibrary.wiley.com/doi/abs/10.1029/2004JE002332 doi: https://doi.org/10.1029/2004JE002332

Nakamura, Y., Latham, G., Dorman, H., & Harris, J. (1981). Passive seismic experiment long-period event catalog. *Galveston Geophysics Laboratory Contribution*, *491*, 314.

Nakamura, Y., Latham, G. V., & Dorman, H. J. (1982a). Apollo lunar seismic experiment—final summary. *Journal of Geophysical Research: Solid Earth*, *87*(S01), A117–A123.

Nakamura, Y., Latham, G. V., & Dorman, H. J. (1982b). Apollo lunar seismic experiment—final summary. *Journal of Geophysical Research: Solid Earth*,

87(S01), A117-A123. Retrieved from https://agupubs.onlinelibrary.wiley.com/doi/abs/10.1029/JB087iS01p0A117 doi: https://doi.org/10.1029/JB087iS01p0A117

Nunn, C., Garcia, R. F., Nakamura, Y., Marusiak, A. G., Kawamura, T., Sun, D., ... others (2020). Lunar seismology: A data and instrumentation review. *Space Science Reviews*, *216*(5), 89.

Panning, M., Kedar, S., Bowles, N., Calcutt, S., Cutler, J., Elliott, J., ... others (2021). Farside seismic suite (fss): First seismic data from the farside of the moon delivered by a commercial lander. In *Agu fall meeting abstracts* (Vol. 2021, pp. P54C–01).

Pedregosa, F., Varoquaux, G., Gramfort, A., Michel, V., Thirion, B., Grisel, O., ... others (2011). Scikit-learn: Machine learning in python. *the Journal of machine Learning research*, *12*, 2825–2830.

Pickrell, J. (2022, May). These six countries are about to go to the moon — here's why. *Nature*, *605*, 208–211. doi: 10.1038/d41586-022-01252-7

Quinlan, J. R. (1986). Induction of decision trees. *Machine learning*, *1*, 81–106.

Rhodes, B. (2019). Skyfield: Generate high precision research-grade positions for stars, planets, moons, and earth satellites. *Astrophysics Source Code Library*, ascl–1907.

Standley, I. M., Pike, W. T., Calcutt, S., & Hoffman, J. P. (2023). Short period seismometer for the lunar farside seismic suite mission. In *2023 ieee aerospace conference* (p. 1-9). doi: 10.1109/AERO55745.2023.10115559

Toksöz, M. N., Dainty, A. M., Solomon, S. C., & Anderson, K. R. (1974). Structure of the moon. *Reviews of Geophysics*, *12*(4), 539-567. Retrieved from https://agupubs.onlinelibrary.wiley.com/doi/abs/10.1029/RG012i004p00539 doi: https://doi.org/10.1029/RG012i004p00539

Toksöz, M. N., Goins, N. R., & Cheng, C. (1977). Moonquakes: Mechanisms and relation to tidal stresses. *Science*, *196*(4293), 979–981.

Turner, A. R., Hawthorne, J. C., & Gaddes, M. (2022). Stresses in the lunar interior: Insights from slip directions in the a01 deep moonquake nest. *Journal of Geophysical Research: Planets*, *127*(12), e2022JE007364. Retrieved from https://agupubs.onlinelibrary.wiley.com/doi/abs/10.1029/2022JE007364 doi: https://doi.org/10.1029/2022JE007364

van der Maaten, L., & Hinton, G. (2008). Visualizing data using t-sne. *Journal of Machine Learning Research*, *9*(86), 2579–2605. Retrieved from http://jmlr.org/papers/v9/vandermaaten08a.html

Weber, R., Bills, B., & Johnson, C. (2009). Constraints on deep moonquake focal mechanisms through analyses of tidal stress. *Journal of Geophysical Research: Planets*, *114*(E5).

Weber, R., Bills, B., & Johnson, C. (2010). A simple physical model for deep moonquake occurrence times. *Physics of the Earth and Planetary Interiors*, *182*(3-4), 152–160.

Weber, R., Neal, C., Grimm, R., Grott, M., Schmerr, N., Wieczorek, M., ... others (2021). The scientific rationale for deployment of a long-lived geophysical network on the moon. *Bulletin of the AAS*, *53*(4).

Witze, A. (2022, May). The $93-billion plan to put astronauts back on the moon. *Nature*, *605*, 212–216. doi: 10.1038/d41586-022-01253-6

Identifying deep moonquake nests using machine learning model on single lunar station on the far side of the Moon

Josipa Majstorović[1], Philippe Lognonné[1], Taichi Kawamura[1], Mark P. Panning[2]

[1]Université Paris Cité, Institut de physique du globe de Paris, CNRS, Paris, France
[2]Jet Propulsion Laboratory, California Institute of Technology, Pasadena, CA, USA

Key Points:

- As a part of the future space mission NASA will deploy a new seismic station to Schrödinger Basin on the far side of the Moon.
- We propose a machine learning model trained to classify deep moonquakes using the lunar orbital parameter.
- The models perform with accuracy greater than 70% when trained to classify combinations of four or fewer nests.

Corresponding author: Josipa Majstorović, josipa.majstorovic@protonmail.com

Abstract

One of the future NASA space program includes the Farside Seismic Suite (FSS) payload, a single station with two seismometers, on the far side of the Moon. During FSS operations, the processing of the data will provide us with new insight into the Moon's seismic activity. One of Apollo mission finding is the existence of deep moonquakes (DMQ), and the nature of their temporal occurrence patterns as well as the spatially clustering. It has been shown that DMQs reside in about 300 source regions. In this paper we tackle how we can associate new events with these source regions using the single station data. We propose a machine learning model that is trained to differentiate between DMQ nests using only the lunar orbital parameters related to DMQ time occurrences. We show that ML models perform well (with an accuracy $> 70\%$) when they are trained to classify less than 4 nests.

Plain Language Summary

The future space missions will provide us with various new lunar data, one of which will be ground vibration measurement. The studies of these measurements from the Apollo era in 70s, showed that Moon can host various events. The most intriguing ones are deep moonquakes (DMQs), which are events associated with the displacement deep within the lunar interior. It has been shown that DMQs occur in the specific locations, which are called nests, and that their temporal occurrence is related to the monthly motion of the Moon around the Earth. In this paper we tackle how we can associate new events from only one station located on the far side of the Moon with these known locations of DMQs. We propose a machine learning model that is trained to classify DMQ nests, only using the information about their temporal occurrences, e.g. time of the event, described in terms of different lunar events. We report that models are performing well (with an accuracy $> 70\%$) when they are trained to classify 4 or fewer nests. This gives us a good first approximation about the nest identification.

1 Introduction

We are at the beginning of a golden age of lunar exploration as many nations, together with private companies, are establishing numerous efforts to obtain new scientific measurement of the Moon (Weber et al., 2021; Pickrell, 2022; Kawamura et al., 2022). In light of this, NASA established the Artemis program which should land a crewed mission at the lunar south pole (Witze, 2022). This would be the first attempt of a crewed landing after the successful Apollo missions in 1970's. Before Artemis missions land on the Moon, NASA has also established the Commercial Lunar Payload Services (CLPS) program to land scientific payloads on the Moon using commercial landers. The Farside Seismic Suite (FSS) is one of the selected payloads, and it will deliver two seismometers to Schrödinger Basin on the far side of the Moon (Panning et al., 2021; Standley et al., 2023; Cutler et al., 2023): one vertical Very BroadBand seismometer, and Short Period sensor, both spare or derived from the SEIS experiment sensors (Lognonné et al., 2019, 2020) from the InSight mission to Mars (Banerdt et al., 2020).

The Apollo missions showed the importance of deploying sensors on the surface of the Moon, since a great deal of our knowledge about the Moon comes from the analysis of data acquired during the Apollo era (Lognonné & Johnson, 2015). Thus, analyzing ground motion measurements provided the community with the first constraints on the lunar interior and the activity at the surface (Nakamura et al., 1982a, 1982b; Khan et al., 2000; Khan & Mosegaard, 2002; Khan et al., 2014; Lognonné et al., 2003; Gagnepain-Beyneix et al., 2006; Weber et al., 2010; Garcia et al., 2011; Kawamura et al., 2017; Garcia et al., 2019; Nunn et al., 2020). It has also revealed that the Moon can host events of various origins, such as shallow and deep moonquakes, meteoroid and artificial impacts (Toksöz et al., 1974; Dainty et al., 1975; Lammlein, 1977a; Nakamura, 1983, 2003, 2005).

Today, we have more than twelve thousands events, out of which the deep moonquakes (DMQs) form the most numerous group (Nakamura et al., 1981; Nakamura, 2005).

DMQs are a distinctive group of seismic events that originate from depths between 700 and 1200 km, at high pressure and temperature conditions, where little brittle deformation is expected. Due to very high waveform similarity between quakes, the DMQs have been clustered into about 300 source regions or nests (Nakamura, 2003). This has interpreted to be a consequence of DMQs occurring repeatedly at the fixed nests, which are located mostly on the near side of the Moon. It has been shown that time occurrence of the DMQs is correlated with the monthly motion of the Moon around the Earth. Thus, DMQ occurrences exhibit tidal periodicities and furthermore, the associated high strain rates might explain brittle processes (Kawamura et al., 2017). However, the real causes of their origins are yet to be discovered. There are two puzzling fact about their origin: a) cyclic tidal stresses, caused by the monthly motion of Moon around Earth, are far less than the estimated confining pressures where DMQs occurs (Cheng & Toksöz, 1978; Minshull & Goulty, 1988a); b) do we need both, tectonic and ambient tidal stresses, to explain their mechanical origin (Frohlich & Nakamura, 2009).

To better constrain the lunar interior and unravel the cause of DMQs, it is important to locate new events and associate them with the known nest locations from Apollo with future lunar missions like FSS. These new observations will add, for each new nest, a new differential $t_s - t_p$ measurement constraining the deep interior with a different epicentral distance. However, due to the mission requirements, it is extremely likely that, at the beginning, we might have only one lunar station at the disposal. Therefore, in this paper we study the problem of DMQ nest identification without using waveform information. This is due to the new location of the recording station, which will not match existing Apollo-era waveform templates due to different propagation paths. We propose a machine learning (ML) model that is trained to identify nests within the set of nests of similar differential travel times. The main features used for the model training are related to the fact that different nests respond differently to lunar cycle.

Very early studies have shown correlation between lunar transient events and position of the Moon related to the Earth (Middlehurst, 1967; Cameron & Gilheany, 1967; Moore, 1968). This further encouraged observations that some moonquakes occur with periods that reflect Earth-Moon-Sun relationship (Ewing et al., 1971). Later, it has been shown that the occurrence of DMQs are related to tidal stress cycles, and correlations between DMQs occurrence times and lunar monthly tidal cycles have been indicated (Lammlein et al., 1974; Toksöz et al., 1977; Lammlein, 1977b; Cheng & Toksöz, 1978; Minshull & Goulty, 1988b). The lunar cycle can be explained with three lunar months: synodic, draconic, anomalistic. Synodic month is the period of lunar phases such as New Moon, First Quarter, Full Moon, Last Quarter. Draconic month is the period between two nodes, ascending or descending, where the nodes are points at which the Moon's orbit plane crosses the ecliptic plane towards which it is inclined of about 5.14°. Anomalistic month is the period between two extreme points, perigee and apogee, since the Moon's orbit approximates an ellipse rather than a circle. Earlier studies counted the number of events per day as a function of time and found 0.5 and 1 month signals in the occurrence times related to anomalistic and draconic period of 27 days (Lammlein et al., 1974; Lammlein, 1977b). The same studies also indicated 206-day and 6-year periods, related to the Sun's perturbation on the lunar orbit and the relative precession of the perigee of the Moon's orbit. Subsequently, many recent papers studied and confirmed tidal periodicities of DMQs and more (Bulow et al., 2005, 2007; Bills et al., 2008; Frohlich & Nakamura, 2009; Weber et al., 2009, 2010; Turner et al., 2022).

Based on the previous papers, it is clear that DMQ nests exhibit some clear temporal patterns in their occurrences, and that these are correlated with Moon-Earth system. Therefore, the open question is whether we can design features which would reflect these temporal patterns and to further use those features to study the nest identifica-

tion with one lunar station. In this paper we tackle the question of defining optimal features and the machine learning model. The paper is organised as follows: first, we discuss data used in the analysis, the existing catalog of DMQ events. Second, we discuss the feature design. Third, we introduce a machine learning model. Fourth, we discuss successes and pitfalls of the machine learning model for nest identification applied to different combination of nests. We conclude how this study can offer some first estimates of the nest location in the future lunar missions.

2 Data

We start with the existing catalog of lunar events (Nakamura et al., 1981), which was updated in 2008 and modified in 2018 (Nunn et al., 2020). Catalog contains a list of events (shallow and deep moonquakes, meteoroid and artificial impacts) with attributes such as date and time of the event occurrence, signal envelope amplitude as measured in mm on a standard plot, data availability per station, and the nest (source) classification for DMQs. It is important to note that the source classification is not an exact location defined by latitude and longitude, rather a result from the waveform cross-correlation and single-link cluster analysis (Nakamura, 2003). This analysis positively clustered around 7k DMQs into 77 nests, where the largest nest is associated with label A1. This nest contains 443 quakes and it is placed on the near side of the Moon.

2.1 Catalog processing: nest sets based on travel time information

Earlier studies published lunar interior models and location of DMQ nests in terms of latitude and longitude by picking P and S travel times on the quake waveforms (Garcia et al., 2019, review of these picks). Using lunar interior models and nest locations we can define nests that are close by in distance if we consider only the t_{sp} travel time measurements. To do so we assume that a) our single lunar station is located on the far side in Schrödinger Basin (FSS landing site at 71.378°S, 138.248°E), b) nests' latitudes and longitudes from (Lognonné et al., 2003), c) calculated P- and S- wave travel times (t_p and t_s, respectively) using lunar velocity model between landing site and locations of DMQ nests. By having t_s and t_p we can calculate $t_{sp} = t_s - t_p$ for all nests and models shown in Figure 1 (see Text S1 and Figure S1 for further explanation). Next, we count for each nest how many there are with the similar t_{sp} travel time measurement assuming a picking error of 5 seconds as shown in Figure 1A, consistent with the average picking error in Lognonné et al. (2003). This count provides us with the different sets S_i, shown in Figure 1A, that contain nests N_j of similar travel times. In other words, if we are able to measure t_s and t_p of the new lunar event with accuracy within 5 seconds, we are not able to differentiate between nests that belong to different sets S_i. Therefore, to further tackle the nest identification problem we proceed to associate each event with a combination of lunar orbital measurements.

2.2 Feature selection based on the lunar orbital information

It has been shown that the DMQ temporal patterns in time occurrences are related to different lunar cycles and that these patterns differ from nest to nest. Three lunar cycles are synodic, draconic, anomalistic, and they all have similar periods, but are marked by different motions, either as the motion between two Full Moons phases, or two nodes, or two apsis, respectively. One can list all the events when Moon is in the Full Moon (New Moon) phase, passing through ascending (descending) node or perigee (apogee) by simply looking at the Moon's ephemeris (Meeus, 1991). To make sure that we take into account the temporal patterns, we design the main three features as a time difference between the time of the quake in the nest and the time of the Moon's Full Moon, ascending node and perigee, denoting it as $\Delta t_{FullMoon}, \Delta t_{AscendingNode}, \Delta t_{Perigee}$, respectively. We can achieve the same effect by taking the other three time axis as referent one (New

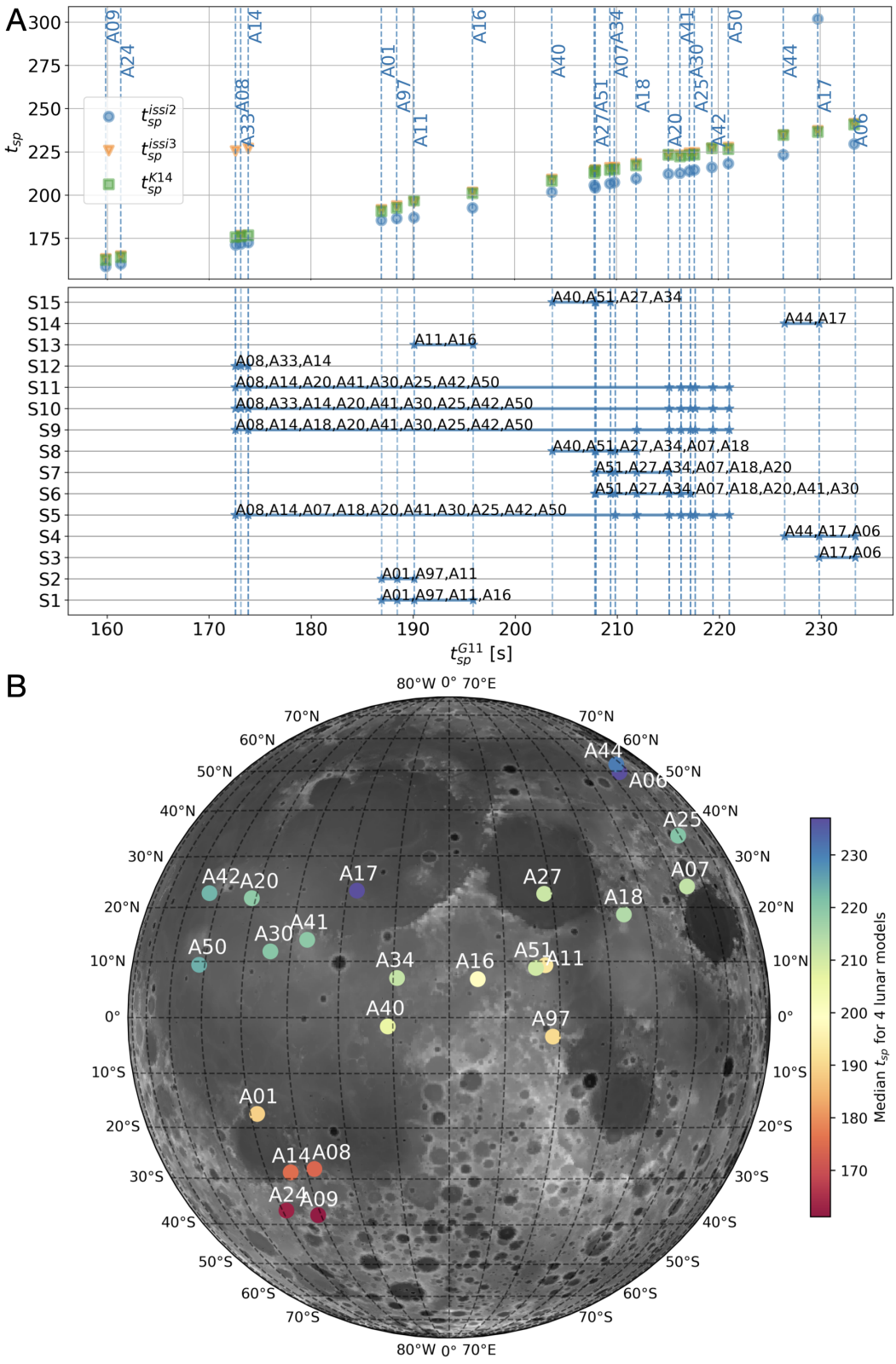

Figure 1. Location study of the DMQ nests from the perspective of $t_{sp} = t_s - t_p$ travel time measurements if we place station in the Schrödinger Basin and consider four different lunar models. A) Upper panel: t_{sp} travel time measurements for four lunar models from Garcia et al. (2011) (G11), Garcia et al. (2019) (issi2, issi3), (Khan et al., 2014) (K14) with nest labels; A) Lower panel: Sets S_i which represent nests with similar travel times if we consider a travel time error of 5 seconds. B) Lunar map with the nests locations where the color indicate the median t_{sp} for four lunar model.

Moon, descending node, and apogee). The next feature is related to the Moon position within its orbit as in Frohlich and Nakamura (2009). The angle between the direction of perigee and the current position of the body, as seen from the main focus of the ellipse, is called the true anomaly, denoted further as γ. Further, as one of the feature we also use the interval time between two quakes in the nest, noted as $e_{i+1} - ei$, as in Weber et al. (2010). And the last two features are related to the position of the Moon with respect to the Earth, and these are the distance, d, itself and the rate of the distance change, $\dot{d}$, as in Bills et al. (2008).

The selected features all have different ranges and we refer to them as raw data. To train a model that is able to generalise well for a given problem sometimes it is necessary to transform raw data to a form that is more suitable for training (Langer et al., 2019). By applying transformation on the raw data we may obtain a mapping which better reveals patterns in our data. Therefore, we chose to apply trigonometric transformation of the true anomaly angle γ, to properly address the jump discontinuities in the feature when angle goes from 2π to 0, due to it's cyclic nature. This is addressed by transforming true anomaly angle γ to pair of $[\cos\gamma, \sin\gamma]$. An example of all eight features are shown in Figure S2 for nest A1.

3 Methodology

When new lunar data arrives, we shall be able to differentiate events in groups based on the waveform similarity measurement. And we shall be able to measure their P and S travel times, and thus form set of nests from Section 2.1. Final step would be to associate these new events with the existing Apollo nests if possible. This nest identification from a single lunar station is a supervised classification problem. The model is trained in a predictive way by taking into account nest locations as labels and nest lunar orbital parameters as input data. Since we want to predict a class (nest), but we do not have statistically large data set (as previously mentioned A1 has 443 quakes), we choose to train a Random Forest (RF) Classifier, since RF can perform well with any size of datasets and tend not to overfit (Ho, 1995; Breiman, 2001).

Random Forest (RF) is a machine learning technique that is based on decision trees (Breiman et al., 1984; Quinlan, 1986) and bootstrap aggregating (Breiman, 1996), where the main output is reached by majority votes among an ensemble of randomised decision trees. A main building unit, a decision tree, is a tree-like learning algorithm where each internal node tests on attribute, each branch corresponds to attribute value and each leaf node represents the final prediction. Usually, during the training phase thresholds, order and number of inequality operations within internal nodes are learned. The hyperparameters that define a RF structure, such as the number of trees, and measure which maximises diversity between classes, are determined beforehand (see Text S2 and Figure S3).

RF also provides an assessment of the feature or input variable importance which might give us an insight of how the model reached its prediction. To assess the feature importance, the RF removes one of the features while it keeps the rest constant, and it measures, among others, the accuracy decrease (Breiman, 2001). RF models are able to solve regression and classification problems, as well as two- and multi-class problems. It has been show that RF can perform with high accuracy even though there are only a few parameters to tune.

In our case, during the training phase, the RF model has access to the extracted features of the individual quakes and the nest labels. The training is performed on a subset of the data, while the model performance is evaluated on the test subset, which the model has never seen. Evaluation is accomplished by comparing the model's predicted class (nest) with the ground truth one. The statistical performance of the model is pre-

sented with confusion matrix and Receiver Operating Characteristic (ROC) curve. We expect that in the case of the ideal RF Classifer the diagonal of the confusion matrix is equal to 1 (and off-diagonal elements are zero), while ROC curve is passing through the left upper corner.

4 Results and discussion

4.1 Training and testing on two largest nests

We first test the hypothesis whether it is possible to differentiate two DMQ nests using the lunar orbital parameters (features). For this, we select the two largest nests, A1 and A8, with a total size of 768 events and ratio A1:A8=$0.57 : 0.43$ (see feature distributions in Figure S4).

Training and testing our base RF model (see Text S2) with the normalised and not normalised input data, we end up selecting to work with the normalised input data since this model performed better (see Figure S5 and S6). The base model trained with the normalised input data performed with an accuracy of 89%, while precision, recall and f1-score for the A1 nest is 88%, 94%, 91%, respectively, and for A8 is 90%, 80%, 85%, respectively (see Figure S6B) with only the occurrence time knowledge. The ROC curve is above the random classifier curve, meaning that the base model is not randomly classifying A1 and A8 nests (see Figure S6C). Out of eight features, the first five most important are $cos(\gamma)$, $\Delta t_{Perigee}$, d, $\Delta t_{AscendingNode}$, $e_{i+1} - e_i$ (see Figure S6D). We notice that $cos(\gamma)$ is the feature with the most important contribution to the model learning. This might be because A1 and A8 have reversed distributions for $cos(\gamma)$ feature (see Figure S 4D).

We proceed into testing learning robustness of our base model in a series of experiments (see Text S2 and Figures S7-S12), all of which indicate that the model is stable. This implies that the base model generalizes well, and not over fit the results. Further, if we examine why the base model sometimes mislabels the nests (Figure S13), we notice that the 2D manifold (see Text S3) of feature space spanned by the input data, calculated by t-sne method (van der Maaten & Hinton, 2008), is not perfectly separated. It seems this segregation might be dominated by a single feature, and that is $\Delta t_{AscendingNode}$ (see Figure S14 and S15A).

4.2 Training and testing on three and more nests

In this section we study how the performance of our base RF model from Section 4.1 changes by adding more nests. We carry out three tests for the next combinations and their ratios: A1-A8-A18 (45%-33%-22%), A1-A8-A18-A6 (38%-28%-18%-15%), A1-A8-A18-A6-A14 (33%-25%-16%-13%-12%), where the three added nests are the three largest nests besides A1 and A8.

The analysis shows that by adding more nests, the performance of our base model deteriorates since the accuracy drops from 88% to 59% (see Figures S16-S19). By adding a 3rd nest, and we notice that A1 and A8 recalls deteriorate slightly, and 50% is A18 events are classified either as A1 or A8 (see Figure S16). Yet, the precision of A18 is the highest. Features, $e_{i+1}-e_i$ and $\dot{d}$, gain importance. Yet, the importance of all features become more equalized. By adding a 4th nest, A6, the recall of A1 nest improves, recall of A8 nest deteriorates even more than before, recall of A18 improves notably, and the new added nest A6 has a recall of 46%, by having most of its events misclassified only as A1 nest, and not a single event as A18 (see Figure S17). This might implies that A18 and A6 nests have completely different source mechanisms. Less notably than before, the importance of all features is becoming more equalized. Lastly, by adding a 5th nest, A14, the recall of A1 and A8 become the highest, and three other nests perform with

recall less than 50%, and their most mislabelled data points are associated with A1 nest (see Figure S18). The importance between features is almost equalized, yet the interval time $e_{i+1} - e_i$ is the only feature that stands out.

These results might imply that by adding more nests, we add more complexity into the problem, since we might be adding nests that have similar source mechanisms. Having similar source mechanisms means that sources are triggered by tides is the same way, so their lunar orbital features have similar characteristics, and we cannot differentiate between nests without having more data. Furthermore, it seems that the only significantly important feature is the interval time, the only feature that does not reflect the lunar orbital information.

Checking the two dimensional representation of the feature space constructed by the feature combination of nests A1-A8-A18-A6-A14, we might conclude that for this particular set it is to some degree impossible to completely differentiate between nests due to the lack of data (see Figure S20).

4.3 Training and testing on nest sets

Using the same base RF model from Section 4.1, we proceed to train and test how well we can differentiate nests that belong to the same set shown in Figure 1. We analyze them in three separate groups by the frequency of the nest they contain: A) S1, S2, S3, S4, S12, S13, S14, S15; B) S5, S6, S7, S8; C) S9, S10, S11. The results are shown in Figure 2A, B, and C, respectively.

We observe high value of recall for most of the nests, as well as high accuracy for most of the sets (see Figure 2). Sets that have $<= 4$ nests perform better than those with more nests, as in sets from group A shown in Figure 2B. When the nest's recall is very low or zero (A11, A30, A41, A42, A50), it signifies a nest with very few events (see ratio of nests in all sets in Figure S18). If we take an example of nest A20, we notice that it has constant recall in many sets (see Figure 2B and C), even though it is not the biggest nest in the set (see Figure S21). Thus, not only the size but probably also the uniqueness of the features determine the success of identifying the nest.

The importance of different features is shown in Figure 3 for all three groups. On one hand, removing just one nest could change the feature importance, as in the case of S2 (where we remove A16) versus S1. On the other hand, we notice that the feature importance does not drastically change when comparing results for sets S3 and S4, where we add nest A44, even though the nest itself is large in size (see Figure S21). For the sets in group B, the feature importance is stable with respect to adding or removing nests. It is quite similar for group C, where only one set S8 has different feature importance. We notice that sets which contain $<= 4$ nests (as in group A), there is usually one or two important features, while for sets with > 4 nests there is equalisation of the feature importance (as in groups B and C). This might imply that a single lunar orbital parameter is enough to explain the occurrence of the nests, which are unique in nature. Mixing more nests suggests that we might be mixing nests with similar temporal patterns, thus learning how to differentiate them is more challenging. Moreover, the feature importance changes for sets that have unique combinations of nests, which may hint that these nests have different source mechanisms.

If we consider a 2D manifold spanned by the sets from groups A, B, C (see Figures S22, S23, S24, respectively), we notice that unique segregation in this space correlates with the RF model accuracy. Nests that form closely spaced homogenized clusters in the 2D manifold tend to be correlated with models that scored high recall for these nests.

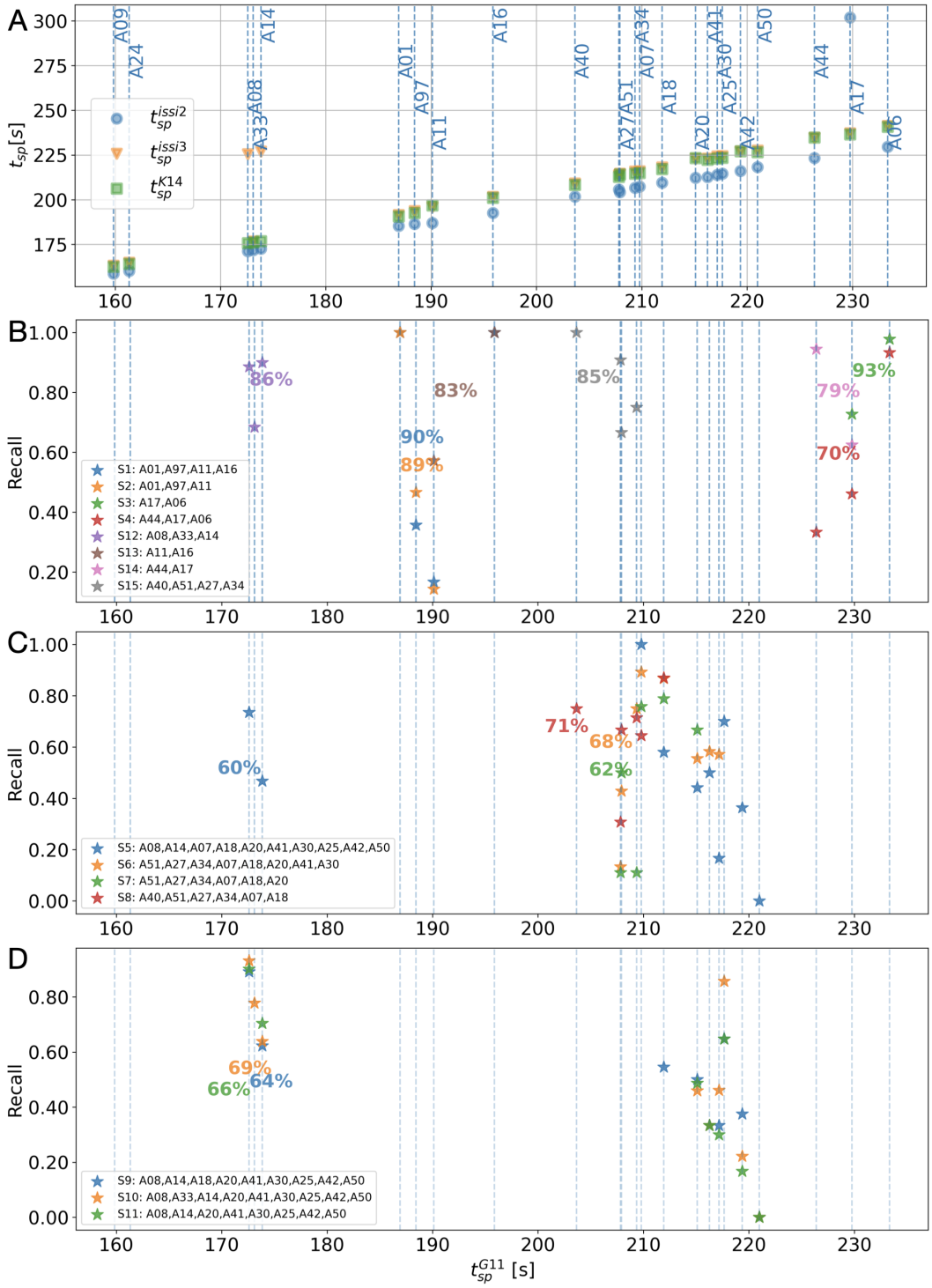

Figure 2. Performance of RF models designed to classify nests within different sets. A) Travel times t_{sp} for four lunar model from Garcia et al. (2011) (G11), Garcia et al. (2019) (issi2, issi3), (Khan et al., 2014) (K14) with nest labels. B) Recall for individual nests within each set with respect to their travel times labeled with sets to which they belong and the scored accuracy of this set. C) and D) same as B) just for different group of sets.

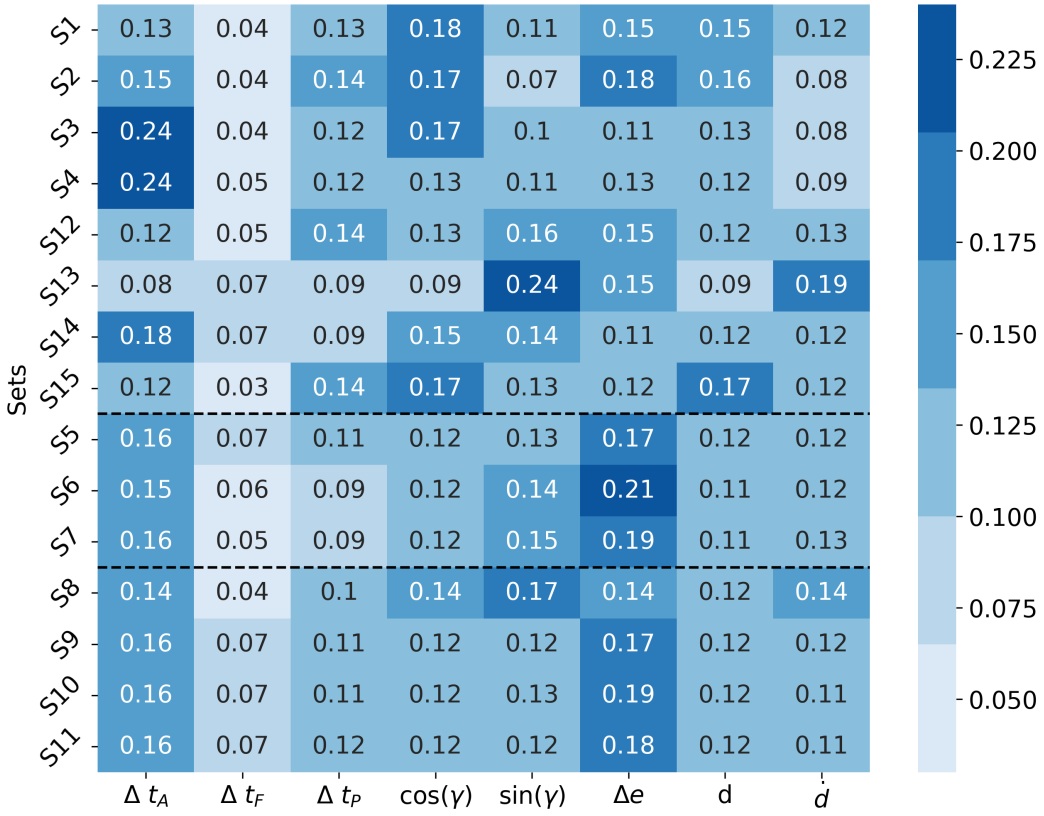

Figure 3. Feature importance for Random Forest models associated with different travel time sets shown in Figure 1.

5 Conclusion

In this paper we propose how to tackle DMQ nest identification during future lunar missions that will likely host only one station on the far side of the Moon. We propose constraining their location by using differential time travel measurement t_{sp} and parameters related to the temporal patterns of the DMQ occurrence. First, in our analysis we assume that we cannot differentiate between nests whose differences in travel time are less than 5 seconds. Thus, we form set of nests that have similar travel times. Second, for each event within the nests we calculate features that are used to build a Random Forest model. This model is trained to differentiate between distinct nests. The features used for training are build by associating each event in all nests with the time difference between events' origin time and time of lunar ascending node, Full Moon phase, perigee, then position of the Moon in its orbit expressed by true anomaly angle, distance of the Moon from the Earth, rate change of this distance, and the time between two successive quakes. We show that by training Random Forest models to differentiate between distinct nests within sets, we can obtain models with high accuracy (more than half of the models score above 70% accuracy). Yet, the performances of these models depend on the number of nests within the set. More nests implies that the problem is more difficult to solve, probably because a) nests might have similar source mechanisms, b) the number of events within nests is unbalanced, and c) we don't have enough data. Since RF models also arrange features by their importance to make a final classification decision, we observe that the importance of the features change with different sets. This complements the findings of previous papers, since it signifies that nests do correspond to different lunar events, which eventually might be connected to the distribution of tidal stresses during these events. Finally, our model provides a good first approximation of the nest identification. And as the catalog of new events grows, it will be straightforward to retrain RF model with the new enlarged dataset.

Open Research Section

The deep moonquake catalog used in this study is published in Nakamura et al. (1981), and revisited in Nunn et al. (2020). Python package Skyfield used to calculate Moon's orbital parameters based on JPL ephemeris can be found on the website `https://rhodesmill.org/skyfield/` (Rhodes, 2019, Software). For our implementation of the Random Forest algorithm we use Scikit-learn machine learning Python library (Pedregosa et al., 2011).

Acknowledgments

French co-authors thanks the French Space Agency, CNES, for supporting this research in the frame of the French contribution to FSS as well as IDEX Paris Cité (ANR-18-IDEX-0001). MPP was supported by funds from the Jet Propulsion Laboratory, under contract with the National Aeronautics and Space Administration (NASA).

References

Banerdt, W. B., Smrekar, S. E., Banfield, D., Giardini, D., Golombek, M., Johnson, C. L., ... others (2020). Initial results from the insight mission on mars. *Nature Geoscience*, *13*(3), 183–189.

Bills, B. G., Bulow, R., & Johnson, C. L. (2008). Influence of earth-moon orbit geometry on deep moonquake occurrence times. *Lunar Planet. Sci., XXXIX*.

Breiman, L. (1996). Bagging predictors. *Machine learning*, *24*, 123–140.

Breiman, L. (2001). Random forests. *Machine learning*, *45*, 5–32.

Breiman, L., Friedman, J., Stone, C. J., & Olshen, R. A. (1984). *Classification and regression trees*. CRC press.

Bulow, R., Johnson, C., Bills, B., & Shearer, P. (2007). Temporal and spatial properties of some deep moonquake clusters. *Journal of Geophysical Research: Planets*, *112*(E9).

Bulow, R., Johnson, C., & Shearer, P. (2005). New events discovered in the apollo lunar seismic data. *Journal of Geophysical Research: Planets*, *110*(E10).

Cameron, W. S., & Gilheany, J. J. (1967). Operation moon blink and report of observations of lunar transient phenomena. *Icarus*, *7*(1-3), 29–41.

Cheng, C. H., & Toksöz, M. N. (1978). Tidal stresses in the moon. *Journal of Geophysical Research: Solid Earth*, *83*(B2), 845-853. Retrieved from `https://agupubs.onlinelibrary.wiley.com/doi/abs/10.1029/JB083iB02p00845` doi: https://doi.org/10.1029/JB083iB02p00845

Cutler, J. W., Nguyen, T. A., Kano, T., Kumar, Y. R. L., Panning, M., April, S., & Haque, S. (2023). Overview of the avionics design for the farside seismic suite. In *Aiaa scitech 2023 forum.* Retrieved from `https://arc.aiaa.org/doi/abs/10.2514/6.2023-1880` doi: 10.2514/6.2023-1880

Dainty, A., Goins, N., & Toksoz, M. (1975). Natural lunar seismic events and the structure of the moon. In *In: Lunar science conference, 6th, houston, tex., march 17-21, 1975, proceedings. volume 3.(a78-46741 21-91) new york, pergamon press, inc., 1975, p. 2887-2897.* (Vol. 6, pp. 2887–2897).

Ewing, M., Latham, G., Press, F., Sutton, G., Dorman, J., Nakamura, Y., ... Kovach, R. (1971). Seismology of the moon and implications on internal structure, origin and evolution. *Highlights of astronomy*, *2*, 155–172.

Frohlich, C., & Nakamura, Y. (2009). The physical mechanisms of deep moonquakes and intermediate-depth earthquakes: How similar and how different? *Physics of the Earth and Planetary Interiors*, *173*(3), 365-374. Retrieved from `https://www.sciencedirect.com/science/article/pii/S0031920109000338` doi: https://doi.org/10.1016/j.pepi.2009.02.004

Gagnepain-Beyneix, J., Lognonné, P., Chenet, H., Lombardi, D., & Spohn, T. (2006). A seismic model of the lunar mantle and constraints on temperature and mineralogy. *Physics of the Earth and Planetary Interiors*, *159*(3-4), 140–166.

Garcia, R. F., Gagnepain-Beyneix, J., Chevrot, S., & Lognonné, P. (2011). Very preliminary reference moon model. *Physics of the Earth and Planetary Interiors*, *188*(1-2), 96–113.

Garcia, R. F., Khan, A., Drilleau, M., Margerin, L., Kawamura, T., Sun, D., ... others (2019). Lunar seismology: An update on interior structure models. *Space Science Reviews*, *215*, 1–47.

Ho, T. K. (1995). Random decision forests. In *Proceedings of 3rd international conference on document analysis and recognition* (Vol. 1, pp. 278–282).

Kawamura, T., Grott, M., Garcia, R., Wieczorek, M., de Raucourt, S., Lognonné, P., ... others (2022). An autonomous lunar geophysical experiment package (algep) for future space missions: In response to call for white papers for the voyage 2050 long-term plan in the esa science program. *Experimental Astronomy*, *54*(2-3), 617–640.

Kawamura, T., Lognonné, P., Nishikawa, Y., & Tanaka, S. (2017). Evaluation of deep moonquake source parameters: Implication for fault characteristics and thermal state. *Journal of Geophysical Research: Planets*, *122*(7), 1487–1504.

Khan, A., Connolly, J. A. D., Pommier, A., & Noir, J. (2014). Geophysical evidence for melt in the deep lunar interior and implications for lunar evolution. *Journal of Geophysical Research: Planets*, *119*(10), 2197-2221. Retrieved from `https://agupubs.onlinelibrary.wiley.com/doi/abs/10.1002/2014JE004661` doi: https://doi.org/10.1002/2014JE004661

Khan, A., & Mosegaard, K. (2002). An inquiry into the lunar interior: A nonlinear inversion of the apollo lunar seismic data. *Journal of Geophysical Research: Planets*, *107*(E6), 3–1.

Khan, A., Mosegaard, K., & Rasmussen, K. L. (2000). A new seismic velocity model for the moon from a monte carlo inversion of the apollo lunar seismic data. *Geophysical Research Letters*, *27*(11), 1591–1594.

Lammlein, D. R. (1977a). Lunar seismicity and tectonics. *Physics of the Earth and Planetary Interiors*, *14*(3), 224-273. Retrieved from https://www.sciencedirect.com/science/article/pii/0031920177901753 doi: https://doi.org/10.1016/0031-9201(77)90175-3

Lammlein, D. R. (1977b). Lunar seismicity and tectonics. *Physics of the Earth and Planetary Interiors*, *14*(3), 224–273.

Lammlein, D. R., Latham, G. V., Dorman, J., Nakamura, Y., & Ewing, M. (1974). Lunar seismicity, structure, and tectonics. *Reviews of Geophysics*, *12*(1), 1–21.

Langer, H., Falsaperla, S., & Hammer, C. (2019). *Advantages and pitfalls of pattern recognition: selected cases in geophysics*. Elsevier.

Lognonné, P., Banerdt, W. B., Giardini, D., Pike, W. T., Christensen, U., Laudet, P., ... others (2019). Seis: Insight's seismic experiment for internal structure of mars. *Space Science Reviews*, *215*, 1–170.

Lognonné, P., Banerdt, W. B., Pike, W. T., Giardini, D., Christensen, U., Garcia, R. F., ... others (2020). Constraints on the shallow elastic and anelastic structure of mars from insight seismic data. *Nature Geoscience*, *13*(3), 213–220.

Lognonné, P., Gagnepain-Beyneix, J., & Chenet, H. (2003). A new seismic model of the moon: implications for structure, thermal evolution and formation of the moon. *Earth and Planetary Science Letters*, *211*(1-2), 27–44.

Lognonné, P., & Johnson, C. (2015). 10.03—planetary seismology. *Treatise on geophysics*, *2*, 65–120.

Meeus, J. (1991). Astronomical algorithms. *Richmond*.

Middlehurst, B. M. (1967). An analysis of lunar events. *Reviews of Geophysics*, *5*(2), 173–189.

Minshull, T., & Goulty, N. (1988a). The influence of tidal stresses on deep moonquake activity. *Physics of the Earth and Planetary Interiors*, *52*(1), 41-55. Retrieved from https://www.sciencedirect.com/science/article/pii/0031920188900568 doi: https://doi.org/10.1016/0031-9201(88)90056-8

Minshull, T., & Goulty, N. (1988b). The influence of tidal stresses on deep moonquake activity. *Physics of the earth and planetary interiors*, *52*(1-2), 41–55.

Moore, P. (1968). Transient lunar phenomena: A review, 1967. *J. Br. Astron. Assoc.*, *78*, 138–144.

Nakamura, Y. (1983). Seismic velocity structure of the lunar mantle. *Journal of Geophysical Research: Solid Earth*, *88*(B1), 677-686. Retrieved from https://agupubs.onlinelibrary.wiley.com/doi/abs/10.1029/JB088iB01p00677 doi: https://doi.org/10.1029/JB088iB01p00677

Nakamura, Y. (2003). New identification of deep moonquakes in the apollo lunar seismic data. *Physics of the Earth and Planetary Interiors*, *139*(3), 197-205. Retrieved from https://www.sciencedirect.com/science/article/pii/S0031920103002103 doi: https://doi.org/10.1016/j.pepi.2003.07.017

Nakamura, Y. (2005). Farside deep moonquakes and deep interior of the moon. *Journal of Geophysical Research: Planets*, *110*(E1). Retrieved from https://agupubs.onlinelibrary.wiley.com/doi/abs/10.1029/2004JE002332 doi: https://doi.org/10.1029/2004JE002332

Nakamura, Y., Latham, G., Dorman, H., & Harris, J. (1981). Passive seismic experiment long-period event catalog. *Galveston Geophysics Laboratory Contribution*, *491*, 314.

Nakamura, Y., Latham, G. V., & Dorman, H. J. (1982a). Apollo lunar seismic experiment—final summary. *Journal of Geophysical Research: Solid Earth*, *87*(S01), A117–A123.

Nakamura, Y., Latham, G. V., & Dorman, H. J. (1982b). Apollo lunar seismic experiment—final summary. *Journal of Geophysical Research: Solid Earth*,

87(S01), A117-A123. Retrieved from https://agupubs.onlinelibrary.wiley.com/doi/abs/10.1029/JB087iS01p0A117 doi: https://doi.org/10.1029/JB087iS01p0A117

Nunn, C., Garcia, R. F., Nakamura, Y., Marusiak, A. G., Kawamura, T., Sun, D., ... others (2020). Lunar seismology: A data and instrumentation review. *Space Science Reviews*, *216*(5), 89.

Panning, M., Kedar, S., Bowles, N., Calcutt, S., Cutler, J., Elliott, J., ... others (2021). Farside seismic suite (fss): First seismic data from the farside of the moon delivered by a commercial lander. In *Agu fall meeting abstracts* (Vol. 2021, pp. P54C–01).

Pedregosa, F., Varoquaux, G., Gramfort, A., Michel, V., Thirion, B., Grisel, O., ... others (2011). Scikit-learn: Machine learning in python. *the Journal of machine Learning research*, *12*, 2825–2830.

Pickrell, J. (2022, May). These six countries are about to go to the moon — here's why. *Nature*, *605*, 208–211. doi: 10.1038/d41586-022-01252-7

Quinlan, J. R. (1986). Induction of decision trees. *Machine learning*, *1*, 81–106.

Rhodes, B. (2019). Skyfield: Generate high precision research-grade positions for stars, planets, moons, and earth satellites. *Astrophysics Source Code Library*, ascl–1907.

Standley, I. M., Pike, W. T., Calcutt, S., & Hoffman, J. P. (2023). Short period seismometer for the lunar farside seismic suite mission. In *2023 ieee aerospace conference* (p. 1-9). doi: 10.1109/AERO55745.2023.10115559

Toksöz, M. N., Dainty, A. M., Solomon, S. C., & Anderson, K. R. (1974). Structure of the moon. *Reviews of Geophysics*, *12*(4), 539-567. Retrieved from https://agupubs.onlinelibrary.wiley.com/doi/abs/10.1029/RG012i004p00539 doi: https://doi.org/10.1029/RG012i004p00539

Toksöz, M. N., Goins, N. R., & Cheng, C. (1977). Moonquakes: Mechanisms and relation to tidal stresses. *Science*, *196*(4293), 979–981.

Turner, A. R., Hawthorne, J. C., & Gaddes, M. (2022). Stresses in the lunar interior: Insights from slip directions in the a01 deep moonquake nest. *Journal of Geophysical Research: Planets*, *127*(12), e2022JE007364. Retrieved from https://agupubs.onlinelibrary.wiley.com/doi/abs/10.1029/2022JE007364 doi: https://doi.org/10.1029/2022JE007364

van der Maaten, L., & Hinton, G. (2008). Visualizing data using t-sne. *Journal of Machine Learning Research*, *9*(86), 2579–2605. Retrieved from http://jmlr.org/papers/v9/vandermaaten08a.html

Weber, R., Bills, B., & Johnson, C. (2009). Constraints on deep moonquake focal mechanisms through analyses of tidal stress. *Journal of Geophysical Research: Planets*, *114*(E5).

Weber, R., Bills, B., & Johnson, C. (2010). A simple physical model for deep moonquake occurrence times. *Physics of the Earth and Planetary Interiors*, *182*(3-4), 152–160.

Weber, R., Neal, C., Grimm, R., Grott, M., Schmerr, N., Wieczorek, M., ... others (2021). The scientific rationale for deployment of a long-lived geophysical network on the moon. *Bulletin of the AAS*, *53*(4).

Witze, A. (2022, May). The $93-billion plan to put astronauts back on the moon. *Nature*, *605*, 212–216. doi: 10.1038/d41586-022-01253-6

Supporting Information for "Identifying deep moonquake nests using machine learning model on single lunar station on the far side of the Moon"

Josipa Majstorović[1], Philippe Lognonné[1], Taichi Kawamura[1], Mark Panning[2]

[1]Université Paris Cité, Institut de physique du globe de Paris, CNRS, Paris, France

[2]Jet Propulsion Laboratory, California Institute of Technology, Pasadena, CA, USA

Contents of this file

1. Text S1 to S3
2. Figures S1 to S24

This file contains supplement text, and figures for the manuscript "Identifying deep moonquake nests using machine learning model on single lunar station on the far side of the Moon". Supplemental Text S1 provides a detailed description of P- and S- travel times calculating for deep moonquake nests using several lunar models. Supplemental Text S2 details about the Random Forest algorithm and the particularity of its training and testing. Supplemental Text S3 provides additional information on the t-distributed stochastic neighbor embedding (t-sne) method. Supplemental Figure S1 show travel time $t_{sp} = t_s - t_p$ for around 20 nests and seven existing lunar models. Supplemental Figure

Corresponding author: J. Majstorović, Université Paris Cité, Institut de physique du globe de Paris, CNRS, Paris, France (josipa.majstorovic@protonmail.com)

S4 illustrates distributions of features used to train machine learning model for two nests, A1 and A8. Supplemental Figure S2 shows features used as an input data for machine learning model. Supplemental Figures S5 to S13 show statistics of the Random Forest models on the test dataset that are trained to dissociate between A1 and A8 nest. Supplemental Figure S13 shows prediction values and negatively labelled data points for the base Random Forest model trained to dissociate between A1 and A8 nests. Supplemental Figure S14 and S15 illustrate 2-D graphic manifold of the space spanned by the 8-D feature space of A1 and A8 nests. Supplemental Figures S16 to S19 show statistic of the Random Forest model trained and tested on combination of nests A1-A8-A18, A1-A8-A18-A6, A1-A8-A18-A6-A14, A8-A18-A6-A14, respectively. Supplemental Figure S20 illustrates 2D graphic manifold representation of the 8D feature space spanned by five nests A1-A8-A18-A6-A14. Supplemental Figure S21 show nests ratios for different sets. Supplemental Figures S22 to S24 illustrates 2-D manifolds of the feature spanned by different sets.

Text S1. Calculation of travel times of seismic waves between sources and station can be obtained using two programming packages: Python package Obspy and its module 'taup' and TauP Java package, both based on the paper Crotwell, Owens, Ritsema, et al. (1999). In our experiment we placed single station on the far side of the Moon in the Schrödinger Crater, while our sources are located nests from the paper Lognonné, Gagnepain-Beyneix, and Chenet (2003). Also, we utilize the existing lunar interior models from papers Garcia et al. (2019) (ISSI 1, ISSI 2, ISSI 3), Garcia, Gagnepain-Beyneix, Chevrot, and Lognonné (2011), Khan, Connolly, Pommier, and Noir (2014), Matsumoto et al. (2015), Weber, Lin, Garnero, Williams, and Lognonné (2011). We first calculate epicentral distances between

nests and station, then travel time of P- and S- seismic waves for the seven models using Python and Java packages. This leaves us with: $t'_{p;i,j}, t'_{s;i,j}, t''_{p;i,j}, t''_{s;i,j}$ where i indicates nest, j indicates lunar model, t' and t'' travel times calculated using Python and Java, respectively. Next, we calculate the average over P- and S- wave travel times for two programming packages, leaving us with $t_{p;i,j} = (t'_{p;i,j} + t''_{p;i,j})/2$, $t_{s;i,j} = (t'_{s;i,j} + t''_{s;i,j})/2$. Further, we calculate the travel time difference, $t_{sp;i,j} = t_{s;i,j} - t_{p;i,j}$ values that we plot in Figure S1, with i running over the y-axis for all nests and j running over the x-axis over all lunar models. We can notice that some combination of nests and lunar models don't have travel time t_{sp} estimation, and some underestimate or overestimate it, when compared to the average value per nest. Due to these discrepancies we decide to further work with only four models: ISSI 2, ISSI 3 Garcia et al. (2019), Garcia PEPI 2011 (Garcia et al., 2011), Khan JGR 2014 (Khan et al., 2014).

Text S2. As discussed in the main manuscript, Random Forest is a machine learning algorithm that consist of ensemble of randomised decision trees. A decision tree consists of decision (internal) nodes, followed by inequality branches, and leaf nodes that hold the final prediction of individual trees shown in Figure S3. Thus, within each tree the beginning is at root node that doesn't have incoming branches. Next in line are internal nodes where based on the available features/attributes and inequality operations, the decision whether the feature is smaller or larger than some threshold is made. These translate to leaf nodes, which represent all possible outcomes. The hyperparamters that define a RF structure and need to be defined before a training process are: the number of decision trees, the maximum depth of trees, the measure that maximises diversity between classes, the minimum samples in the internal node, and the minimum number of samples in leaf

node for it to be considered, the maximum number of features when looking for the best split, the maximum number of leaf nodes, the maximum samples to be draw from the main training dataset when training each decision tree. We proceed to test the learning robustness of our base model that is trained with normalised features (shown in Figure S6) by carry out several experiments: a) changing the randomness of the bootstrapping initialization of the samples that are used when building decision trees, the randomness of the feature sampling when considering for the best split at each internal node, as well as the randomness of the training and test dataset split (see Figure S7); b) changing the optimal number of decision trees (see Figure S8); c) equalizing the size of nests within the dataset by randomly downsampling the largest nest A1 to be the same size as A8 (see Figure S9); d) reducing the number of input feature data to five most important from the base model ($cos(\gamma)$, $\Delta t_{Perigee}$, d, $\Delta t_{AscendingNode}$, $e_{i+1} - e_i$) (see Figure S10). In all test beside those in experiment a), we keep the random state fixed. Finally, the results do not vary between different tests, indicating that in all above configurations models are able to learn how to classify two nest with the similar performances. Further, we notice that in experiment c) the statistic for A8 nest improved compared to the base model statistic, indicating that having a balanced classes while training a ML is important. Moreover, we observe that the model trained with the fewer features statistically perform worst than the base model. This might be because all eight features are uncorrelated, thus equally important for model learning. Next, we cross-validate our base model. A cross-validation is a technique to assess how the model will generalize to an independent data set by using the resampling technique. A resampling technique uses different portions of the training data to train and validate model during several iteration. Usually, the training

dataset is divided into k equally sized folds, and then k iterations is performed. In each iteration $(k-1)$ folds are used for training, and one fold is used for validation. During the cross-validation, the test set is kept aside. Eventually, the full dataset is divided into three sets: training (55%), validation (20%), test (25%), where training and validation set change in each iteration. We calculate cross-validation with $k = 5$, while keeping the base model parameters. The choice of $k = 5$, has been proven to be a good practice (Witten & James, 2013). This test produces 5 models with the same performance as indicated with ROC curves (see Figure S11). This implies that the base model generalizes well, and to not over fit the results. Moreover, we also perform the grid search over several other RF parameters, besides the number of decision trees. Grid search represents a set of many models, where each model is build with unique set of parameters, and each is trained and tested with the same datasets. The tested parameters are: the maximum features ('auto','sqrt'), the maximum depth of the decision trees (10, 20, 30, 40, 50, 60, 70, 80, 90, 100, 110, None), the minimum samples in the internal nodes (2, 5, 10), the minimum number of samples in leaf node (1, 2, 4), the bootstraping technique on or off. However, it seems that the model that performed the best during the grid search (the minimum samples in internal node equal to 10, the minimum samples in leaf node equal to 2, the maximum features equal to 'auto', the maximum depth equal to 110, with bootstraping turned on) does not perform better than our base model (see Figure S12). Even though our base RF model as a final output predicts a class (A1 or A8), it also associates each class prediction with the class probability. This value ranges between 0 and 1, where 1 indicated that a model is absolutely certain that a given event belongs to a predicted class. From our base model the correctly predicated classes score 81% cases higher than

0.80 for test dataset (see Figure S13A). This suggest that model is confident in its prediction. The mislabelled prediction values show uniform distribution of values between 0.5 to 1 (see Figure S13B). We can further examine these mislabelled events from the perspective of the feature input data. We choose three features, $cos(\gamma)$, $\Delta t_{Perigee}$, d, with high importance value. We could argue that the mislabelled data points from both nests show characteristics which better suits the opposite class (see Figure S13C-E). Yet, the decision is not defined using only one feature. To gain an insight how all eight features contribute into separating two nests, we calculate the 2D manifold of their feature space using t-sne method (van der Maaten & Hinton, 2008). Visualisation of the feature space that is color-coded based on two nests, show us that two classes are well but not perfectly separated (see Figure S14). If we further color 2D manifold space with the values of the individual features, we notice that $\Delta t_{AscendingNode}$ feature might be the most responsible for imperfect split between nests (see Figure S15).

Text S3. One of the statistical dimensionality reduction algorithm that helps to visual high-dimensional data is t-distributed Stochastic Neighbor Embedding (t-sne) algorithm (van der Maaten & Hinton, 2008). It is an unsupervised non-linear reduction technique, since it allows us to separate data that cannot be separated by any straight line. Once it is applied on the input data, first, it starts by calculating the probability distribution of neighbours around each points. The term neighbour stands for the set of points that are closest to a given point. In the input original high-dimensional space the probability is modeled as a Gaussian distribution. Second, the algorithm models the probability of neighbours around given points in the lower-dimensional space using a Student's t-distribution. Third, the algorithm minimizes the divergence, usually Kullback–Leibler

divergence, between two probabilities using gradient descent. The result is a lower-dimensional manifold of the data, that still preserves the pairwise similarities between original data points, optimized to a stable state. This optimisation process generates clusters and sub-clusters of similar data points that become visually better understand in the lower-dimensional space by keeping the relationship of the data from the higher-dimensional space. There are several t-sne hyperparameters that need to be adjusted by the user, and the most importnat one is perplexity. The preplexity parameter defines the number of influential neighbours used to calculate the Gaussian probabilities around given point in the high-dimensional space. Its value range from 5 - 50 (Wattenberg et al., 2016), and can significantly impact the resulting mapping of the input data. For our implementation of the t-sne algorithm we use Scikit-learn machine learning Python library (Pedregosa et al., 2011). After trying some combinations we choose to work with the given set of parameters: n_components=2, perplexity=30, n_iter=5000, verbose=1, random_state=133, while keeping the rest of the them as default by the package implementation.

References

Crotwell, H. P., Owens, T. J., Ritsema, J., et al. (1999). The taup toolkit: Flexible seismic travel-time and ray-path utilities. *Seismological Research Letters*, *70*, 154–160.

Garcia, R. F., Gagnepain-Beyneix, J., Chevrot, S., & Lognonné, P. (2011). Very preliminary reference moon model. *Physics of the Earth and Planetary Interiors*, *188*(1-2), 96–113.

Garcia, R. F., Khan, A., Drilleau, M., Margerin, L., Kawamura, T., Sun, D., ... others (2019). Lunar seismology: An update on interior structure models. *Space Science Reviews*, *215*, 1–47.

Khan, A., Connolly, J. A. D., Pommier, A., & Noir, J. (2014). Geophysical evidence for melt in the deep lunar interior and implications for lunar evolution. *Journal of Geophysical Research: Planets*, *119*(10), 2197-2221. Retrieved from `https://agupubs.onlinelibrary.wiley.com/doi/abs/10.1002/2014JE004661` doi: https://doi.org/10.1002/2014JE004661

Lognonné, P., Gagnepain-Beyneix, J., & Chenet, H. (2003). A new seismic model of the moon: implications for structure, thermal evolution and formation of the moon. *Earth and Planetary Science Letters*, *211*(1-2), 27–44.

Matsumoto, K., Yamada, R., Kikuchi, F., Kamata, S., Ishihara, Y., Iwata, T., ... Sasaki, S. (2015). Internal structure of the moon inferred from apollo seismic data and selenodetic data from grail and llr. *Geophysical Research Letters*, *42*(18), 7351-7358. Retrieved from `https://agupubs.onlinelibrary.wiley.com/doi/abs/10.1002/2015GL065335` doi: https://doi.org/10.1002/2015GL065335

Pedregosa, F., Varoquaux, G., Gramfort, A., Michel, V., Thirion, B., Grisel, O., ... others (2011). Scikit-learn: Machine learning in python. *the Journal of machine Learning research*, *12*, 2825–2830.

van der Maaten, L., & Hinton, G. (2008). Visualizing data using t-sne. *Journal of Machine Learning Research*, *9*(86), 2579–2605. Retrieved from http://jmlr.org/papers/v9/vandermaaten08a.html

Wattenberg, M., Viégas, F., & Johnson, I. (2016). How to use t-sne effectively. *Distill*. Retrieved from http://distill.pub/2016/misread-tsne doi: 10.23915/distill.00002

Weber, R. C., Lin, P.-Y., Garnero, E. J., Williams, Q., & Lognonné, P. (2011). Seismic detection of the lunar core. *Science*, *331*(6015), 309-312. Retrieved from https://www.science.org/doi/abs/10.1126/science.1199375 doi: 10.1126/science.1199375

Witten, D., & James, G. (2013). *An introduction to statistical learning with applications in r*. springer publication.

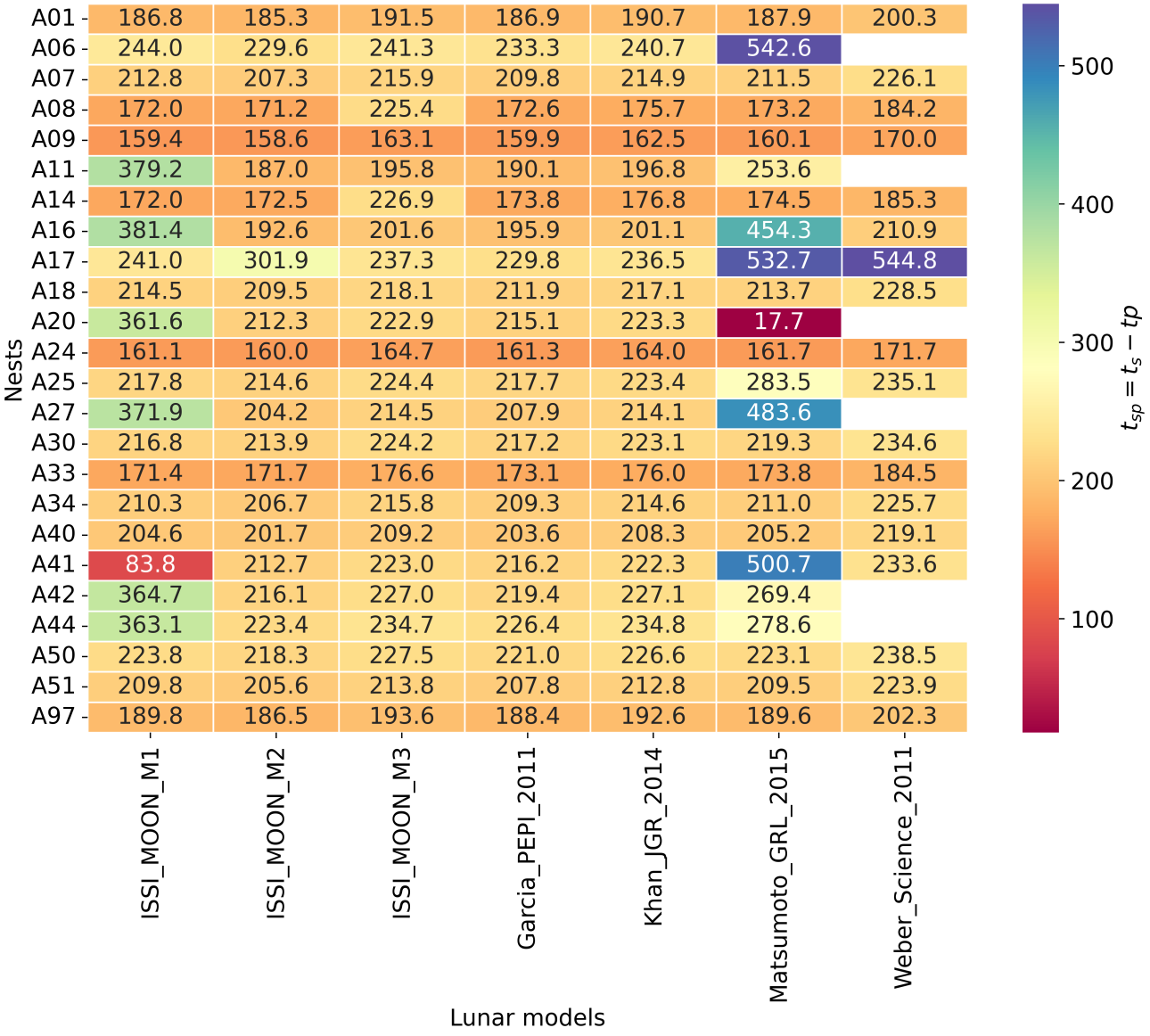

Figure S1. Travel time $t_{sp} = t_s - t_p$ calculations, where t_s and t_p stands for S- and P- waves travel times, respectively, between the range of nests and the station placed on the far side of the Moon in the Schrödinger crater. Calculation are done for seven existing lunar model, from papers Garcia et al. (2019) (ISSI M1, ISSI M2, ISSI M3), Garcia et al. (2011), Khan et al. (2014), Matsumoto et al. (2015), Weber et al. (2011).

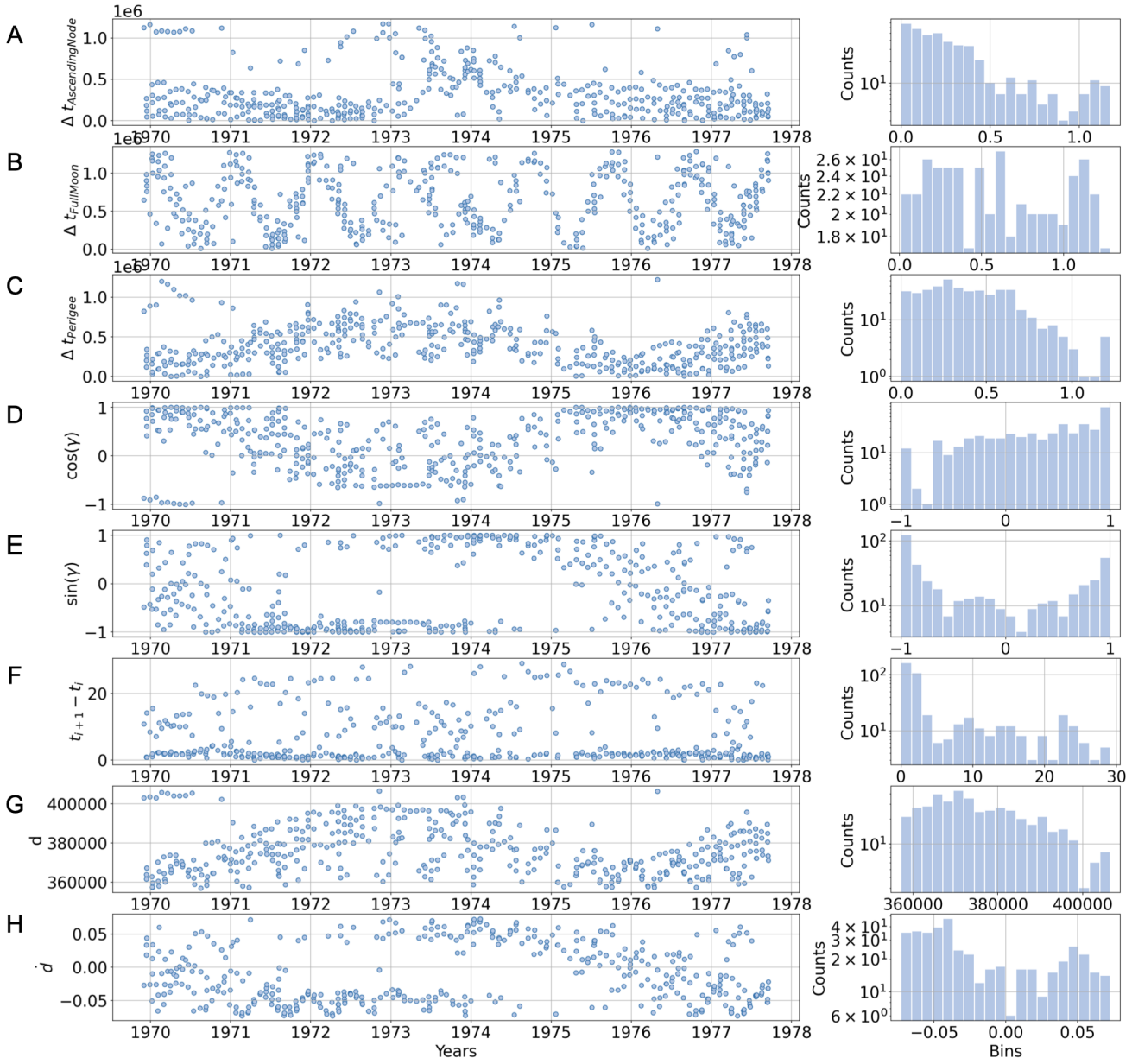

Figure S2. Time evolution of features during the Apollo mission and their histograms for A1 nest. First three features are time difference between quakes and A) the instance when Moon was passing through ascending node, B) Full Moon phase, C) instance when Moon was in perigee; next D) $\cos\gamma$, E) $\sin\gamma$ where γ is the true anomaly angle, indicating the position of the Moon in the orbit; F) time difference between two quakes, G) distance between Moon and Earth at the quake occurrence, H) the rate of distance change from G.

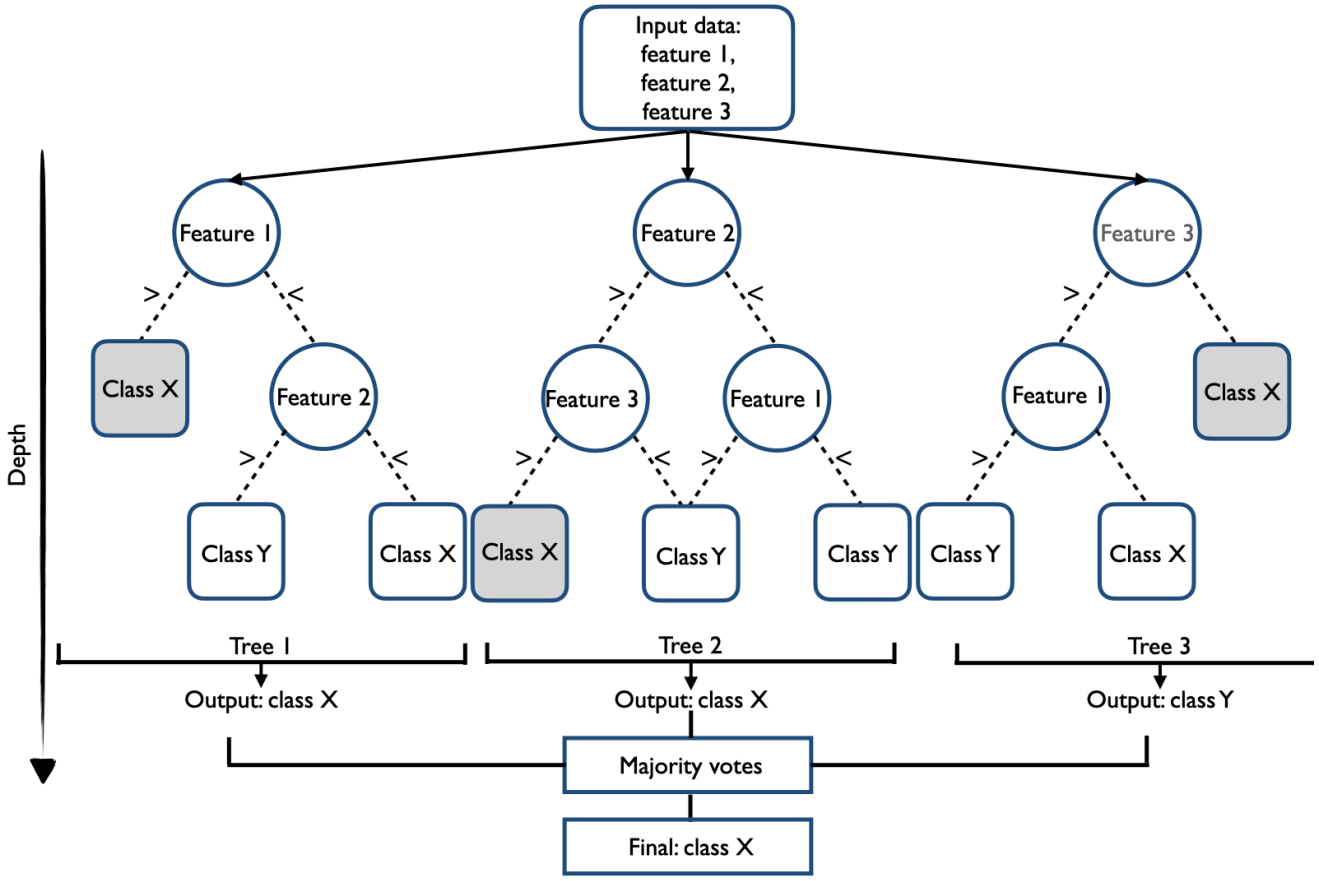

Figure S3. Schematic representation of a Random Forest algorithm. In this example, the model is trained with 3 features, it consists of 3 decision trees with a maximum tree depth equal to 3. A tree consists of decision nodes (circles), followed by inequality branches (dashed lines) , and leaf nodes (rectangles). The prediction is taking place in each tree by yes or no questions, while the final prediction is made upon majority voting considering individual tree predictions.

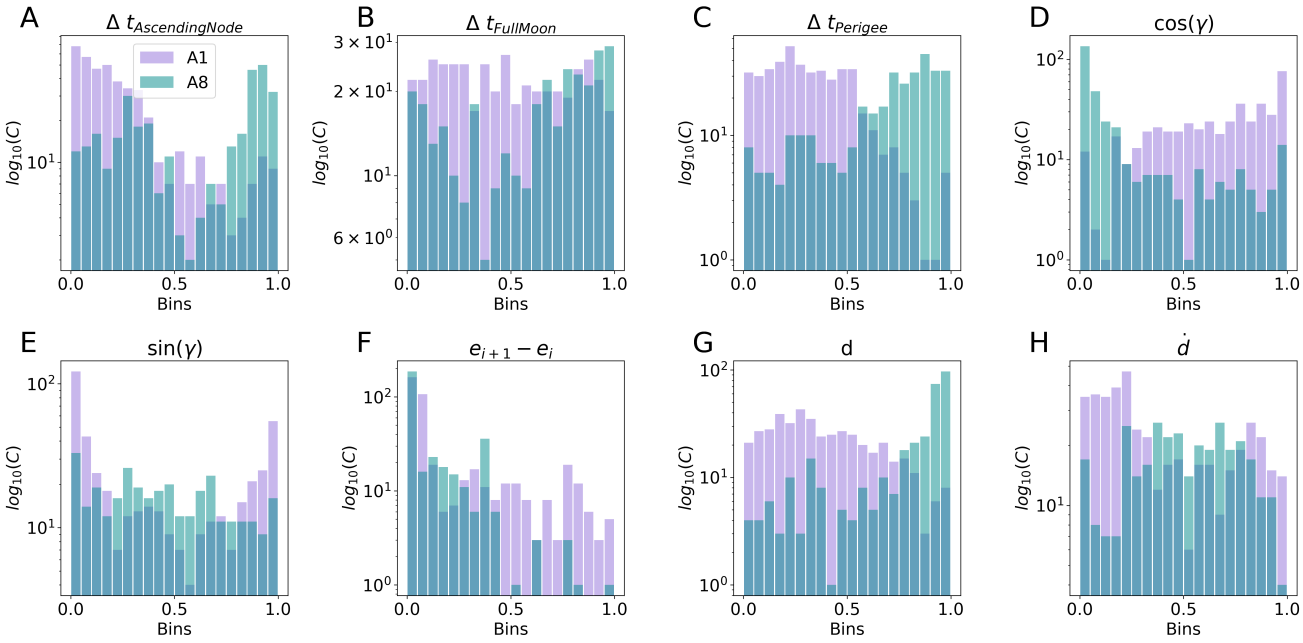

Figure S4. Distributions of eight features used for training Random Forest model for dissociating between nests A1 and A8.

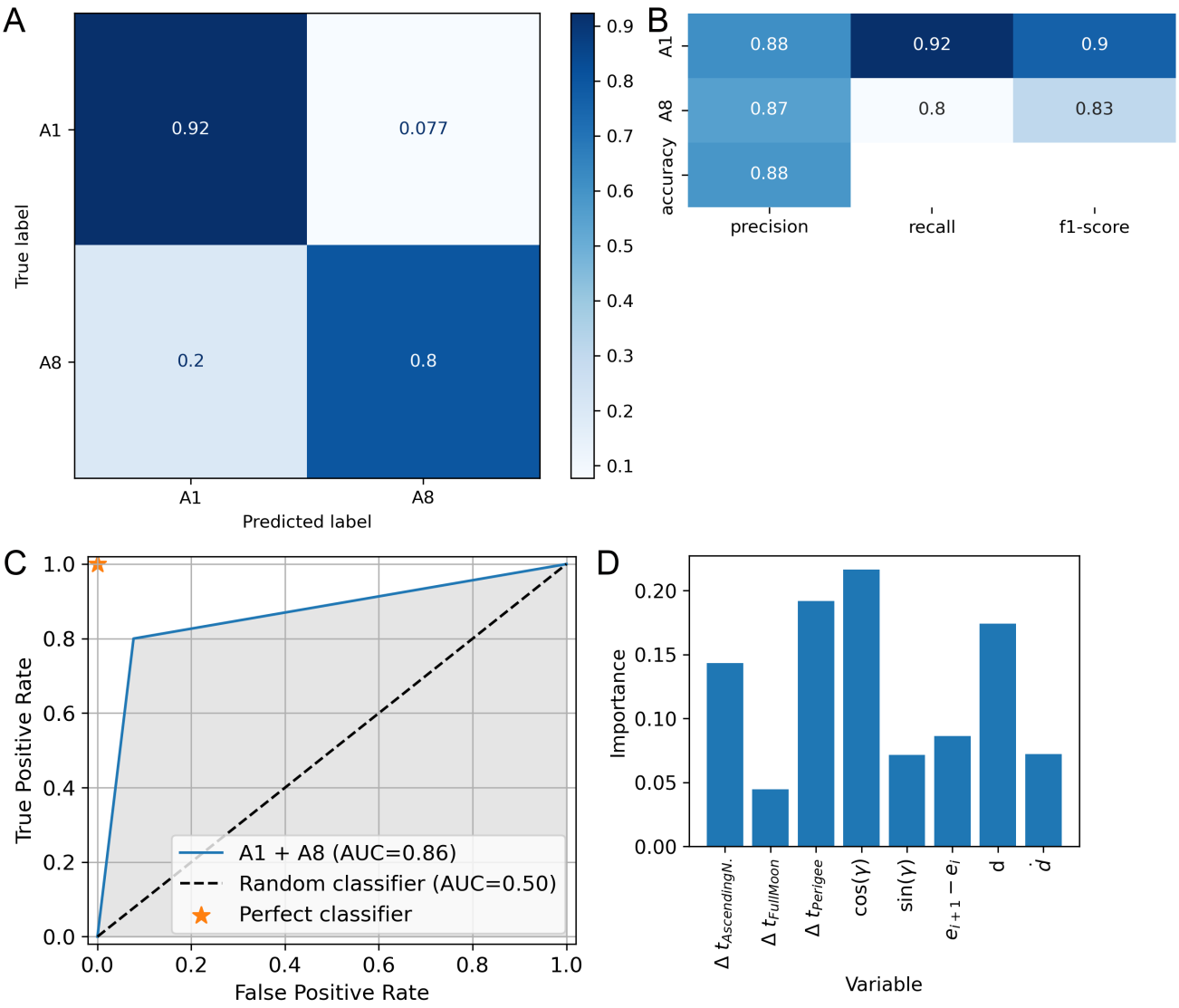

Figure S5. Statistics performance of the base Random Forest model on the dataset trained to dissociate between nests A1 and A8 using raw feature data without normalisation: A) confusion matrix, B) precision, recall, f1-score per nests and accuracy of the model, C) receiver operating characteristic (ROC) curve, D) feature importance for the model to make decisions.

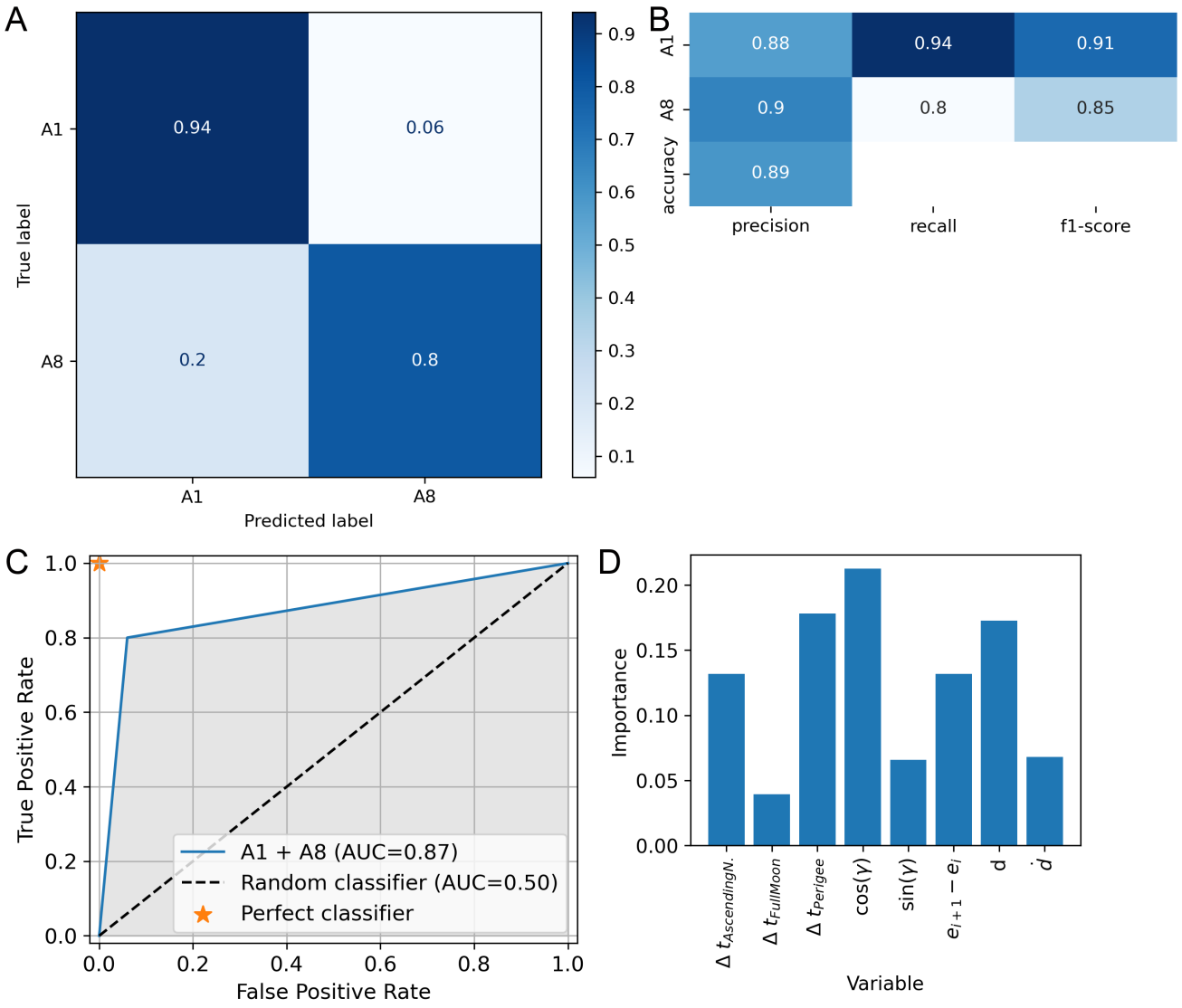

Figure S6. Same as Figure S5 but using feature data that are normalised between 0 and 1.

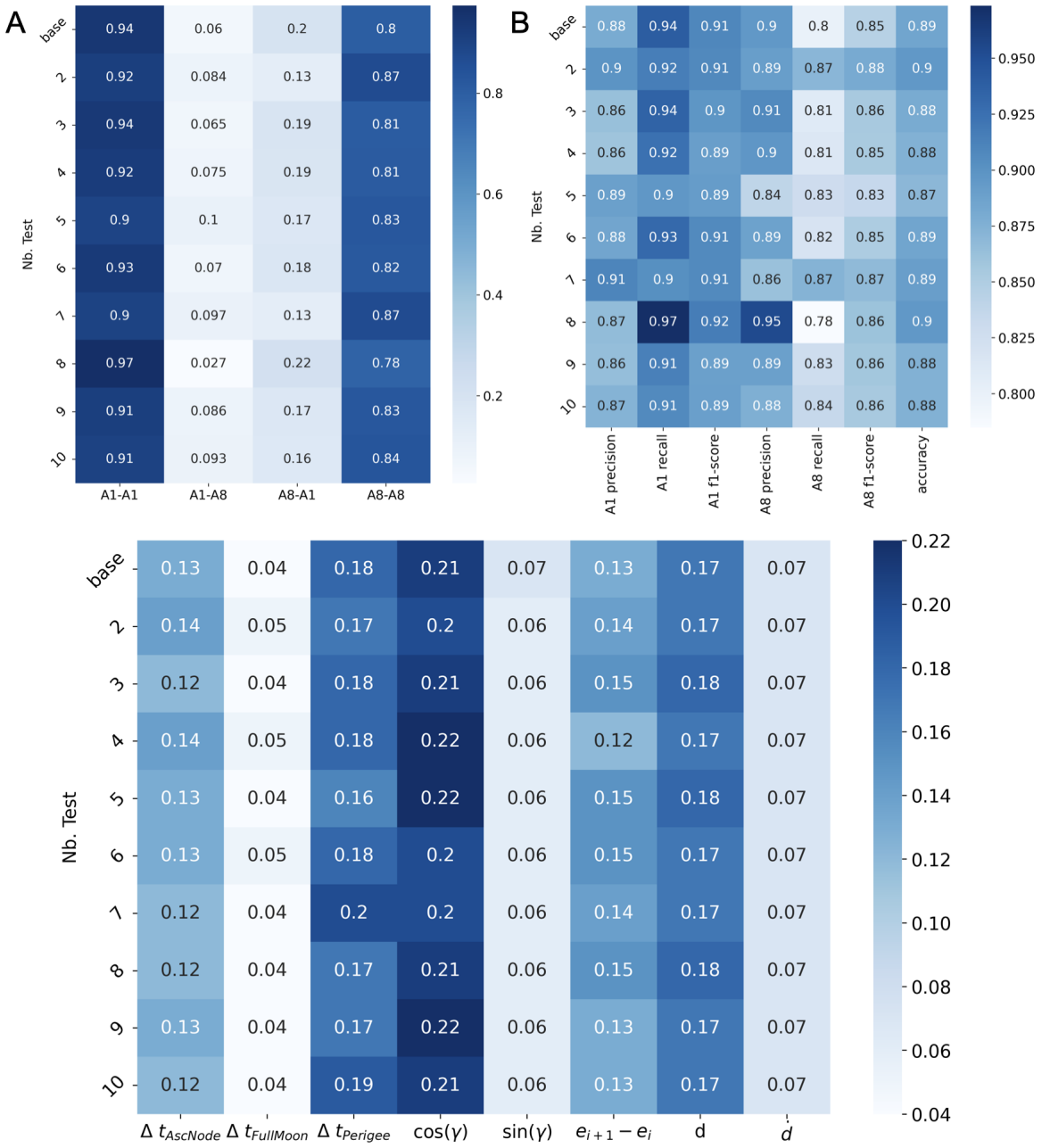

Figure S7. Statistics performance of the Random Forest models while changing the randomness of the data split and decision tree initialisation compared to the base model shown in Figure S6. The models are trained to dissociated between nests A1 and A8. The randomness is changed from 600 to 1400 from test 1 to test 10 by step of 100. Statistics are: A) confusion matrix, B) precision, recal, f1-score and accuracy of the model, C) the importance of the feature used by the models to make a correct classification.

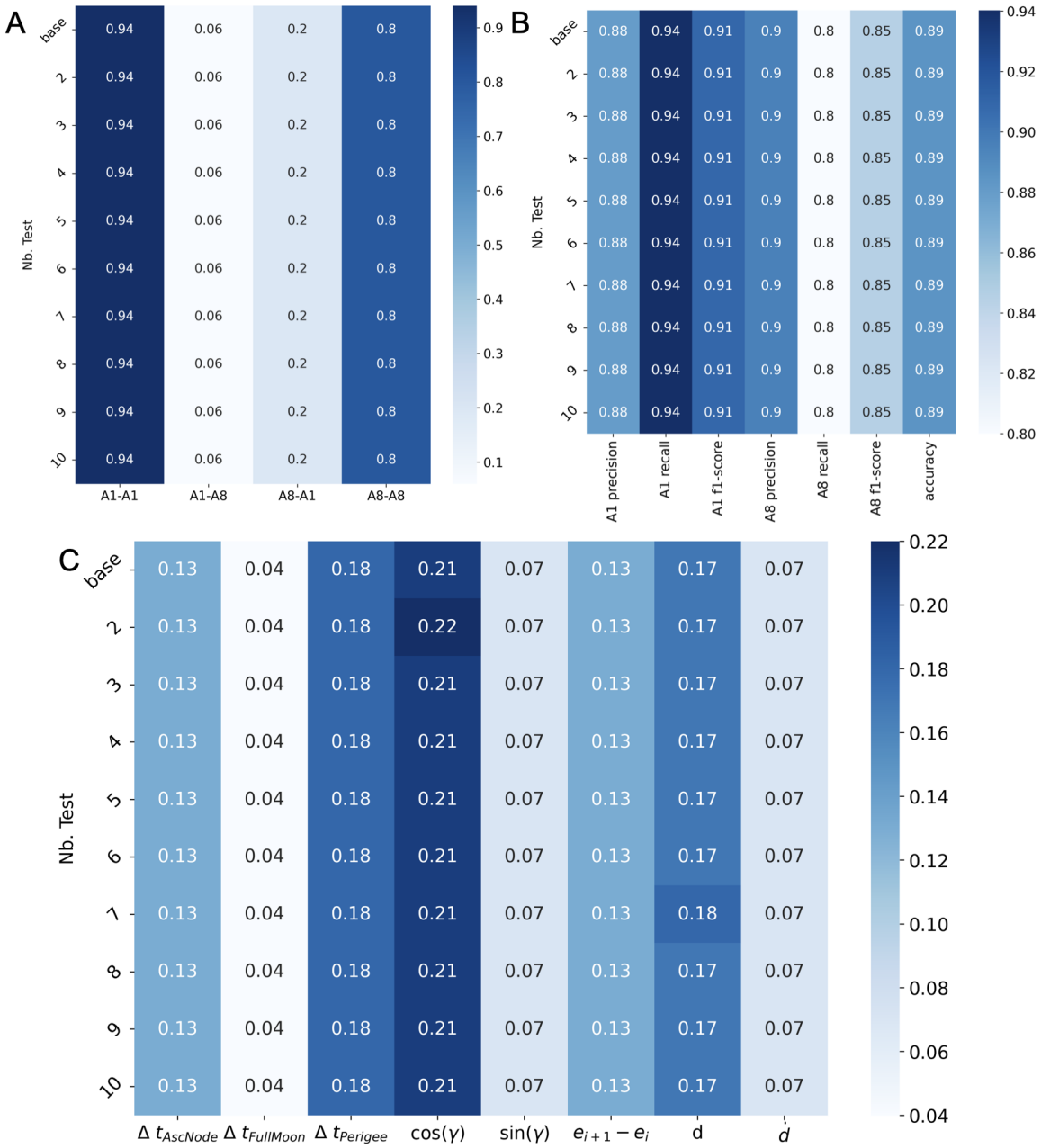

Figure S8. Same as Figure S7 while keeping the randomness fixed, but changing the number of trees used to build Random Forest model.

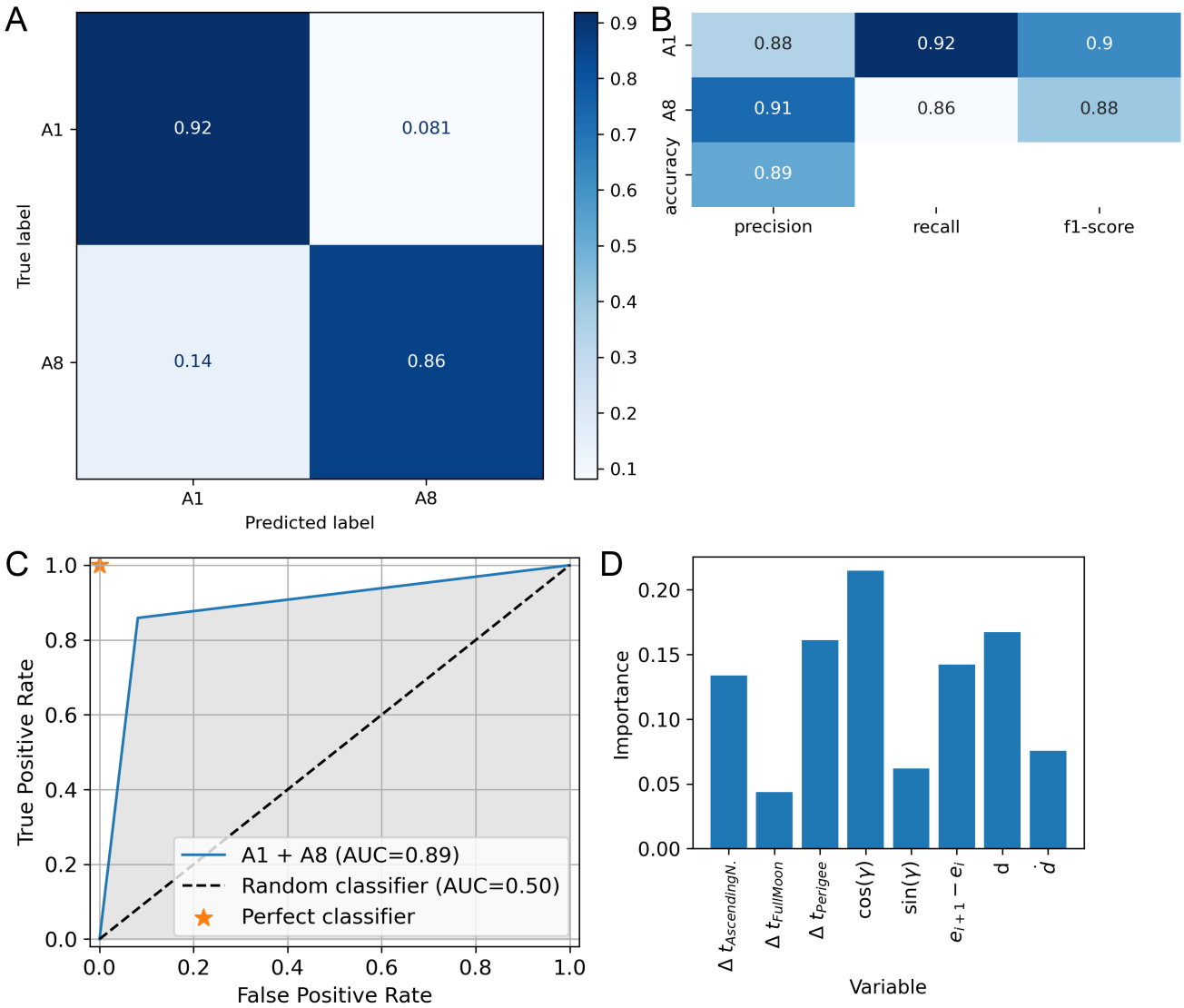

Figure S9. Same as Figure S6, but using the balanced dataset, thus having the same number of A1 and A8 events.

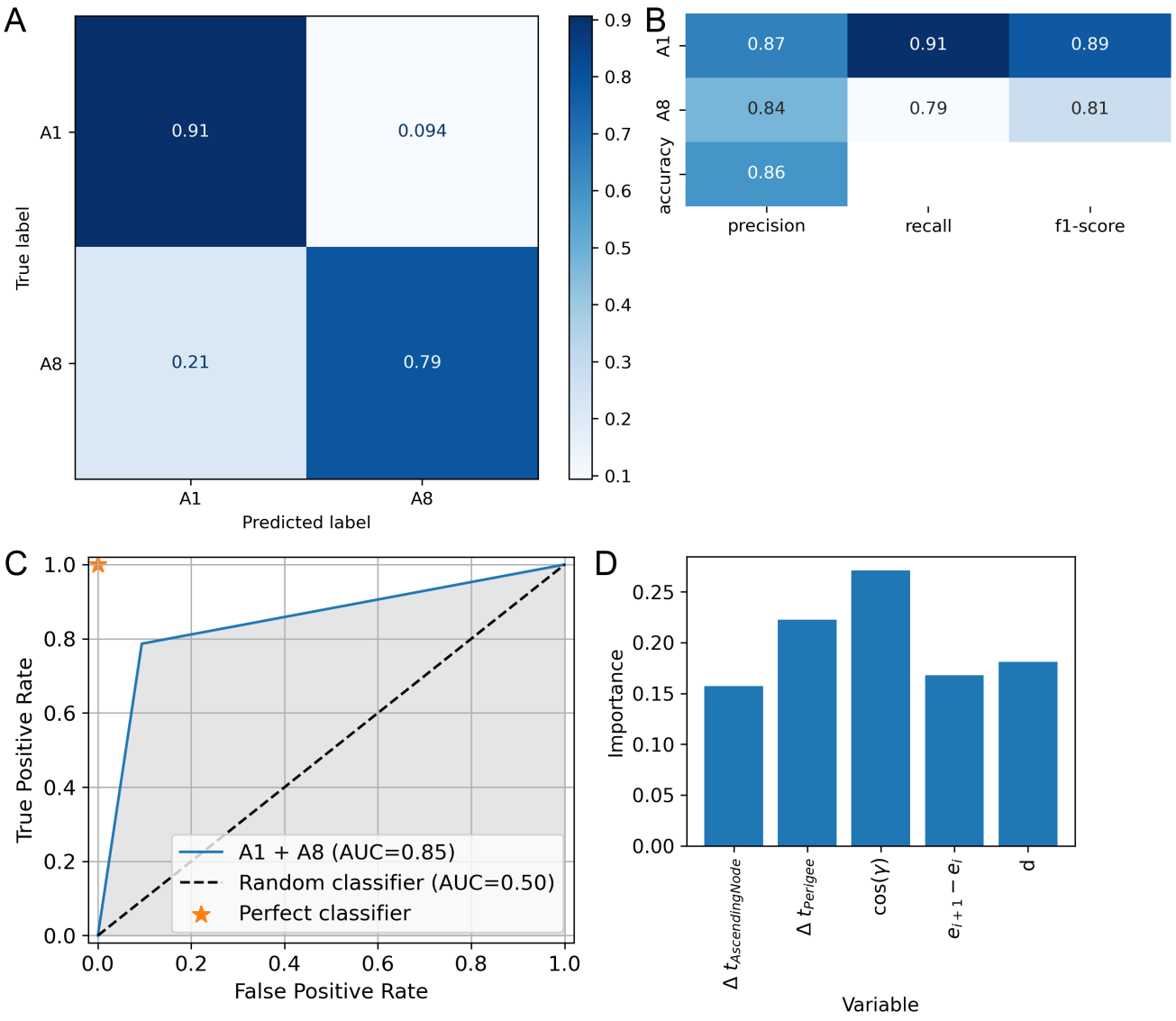

Figure S10. Same as Figure S6, but keeping only five out of eight features: $\Delta t_{AscendingNode}$, $\Delta t_{Perigee}$, $\cos(\gamma)$, $e_{i+1} - e_i$, d.

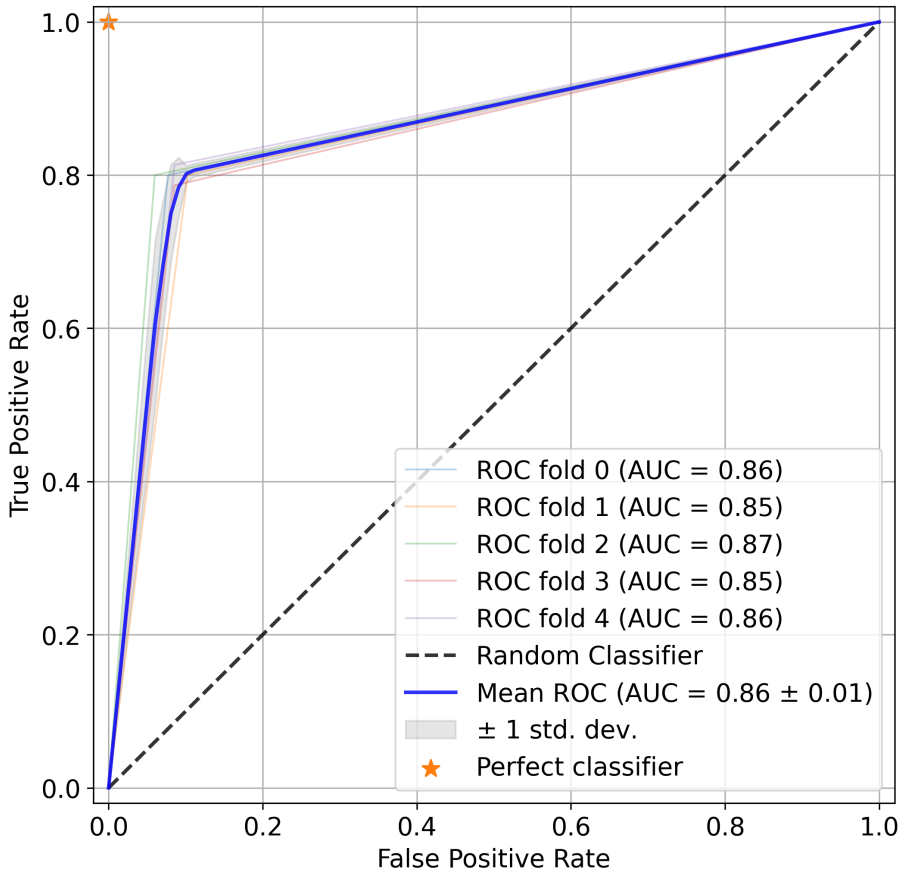

Figure S11. 5-fold cross-validation of the base RF model shown in Figure S6 with the mean and standard deviation.

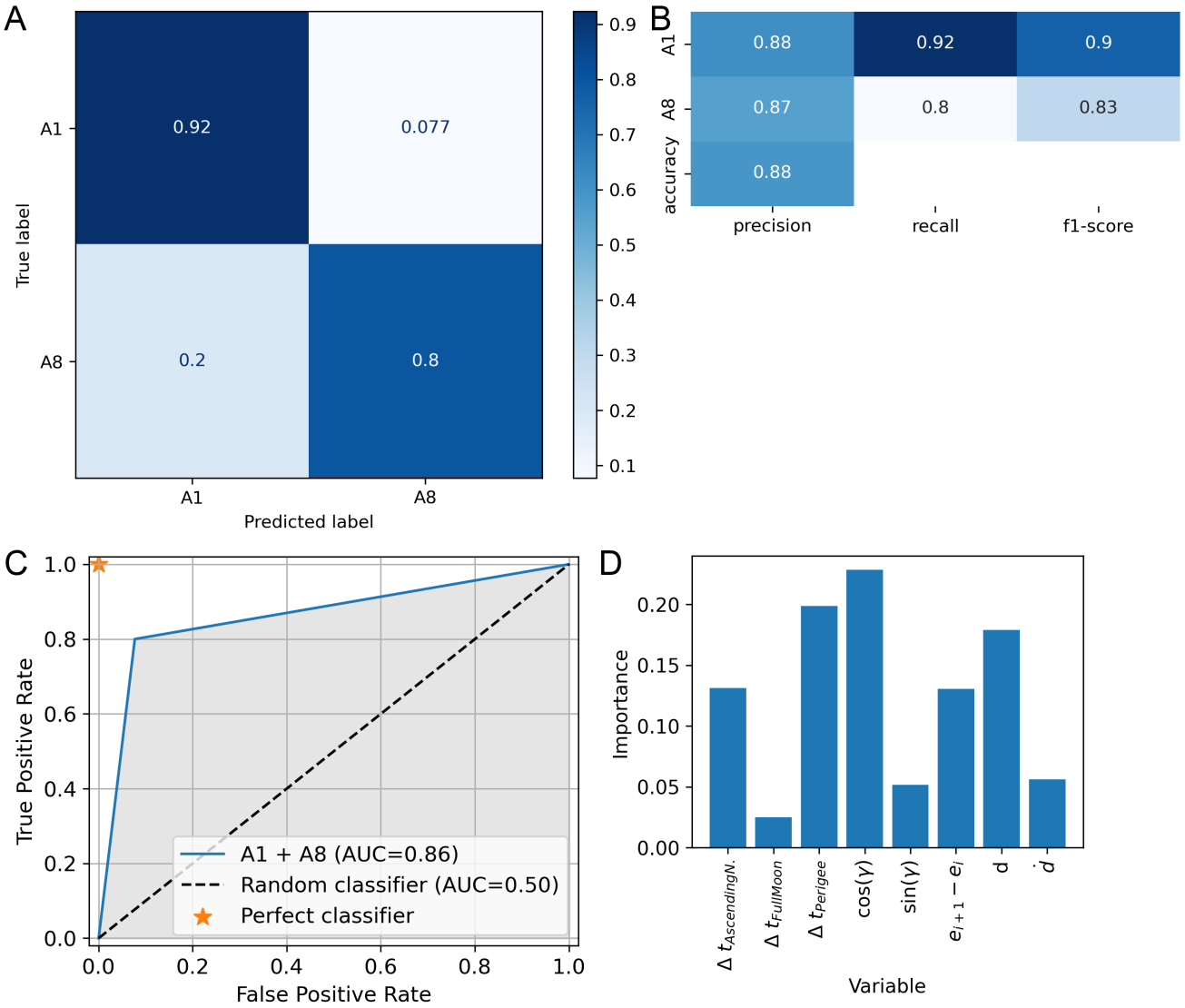

Figure S12. Same as Figure S6, but for the best performing model from the grid search analysis.

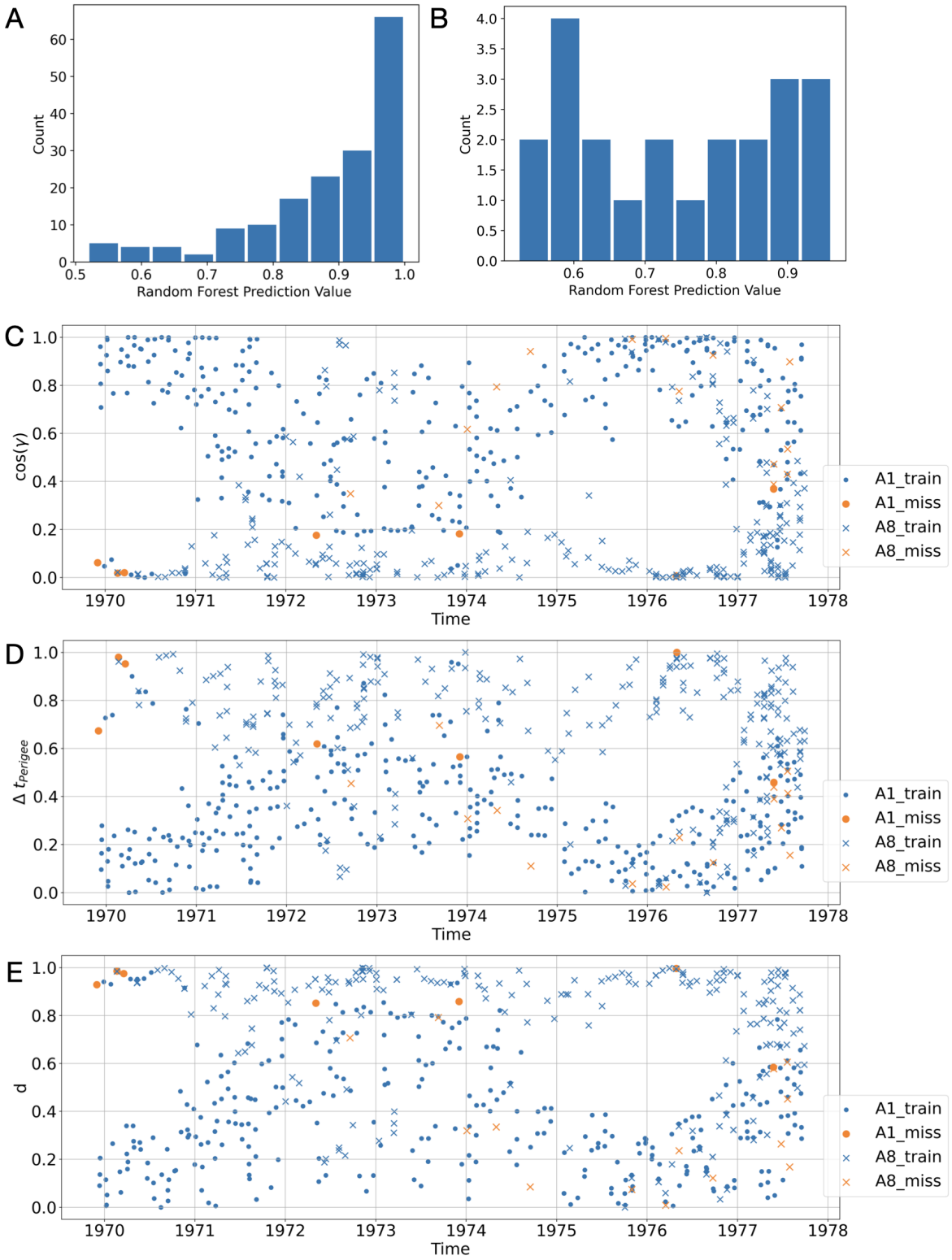

Figure S13. Classification results: A) prediction values for positively classified events, B) prediction values for negatively classified events. Events used for training and events used for testing but got mislabeled form the perspective of features: C) $\cos(\gamma)$, D) $\Delta t_{Perigee}$, E) d.

Figure S14. 2-D manifold of the feature space spanned by nests A1 and A8.

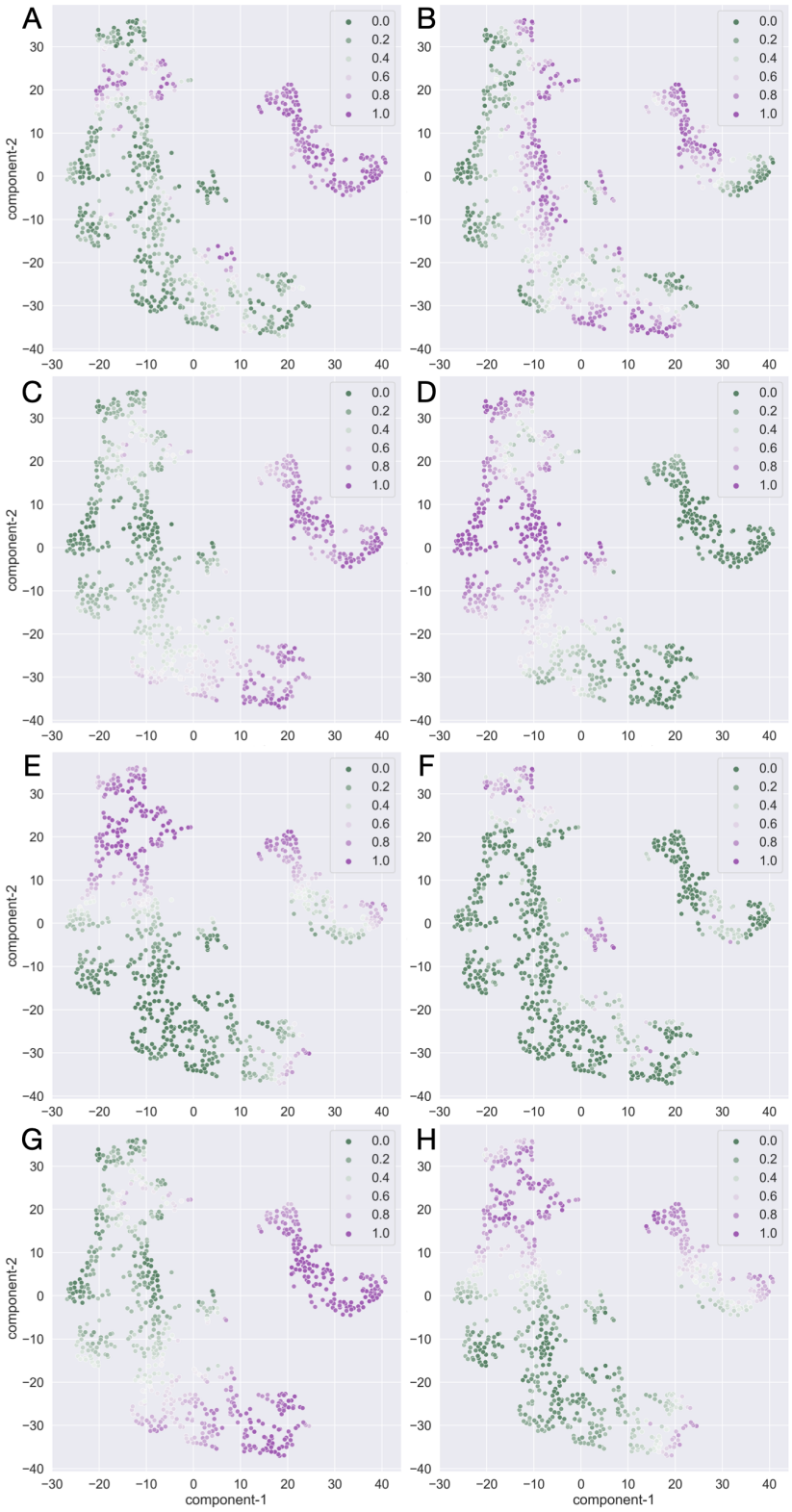

Figure S15. 2-D manifold of the feature space spanned by nests A1 and A8 colored by the features: A) $\Delta t_{AscendingNode}$, B) $\Delta t_{FullMoon}$, C) $\Delta t_{Perigee}$, D) $\cos(\gamma)$, E) $\sin(\gamma)$, F) $e_{i+1} - e_i$, G) d, H) $\dot{d}$.

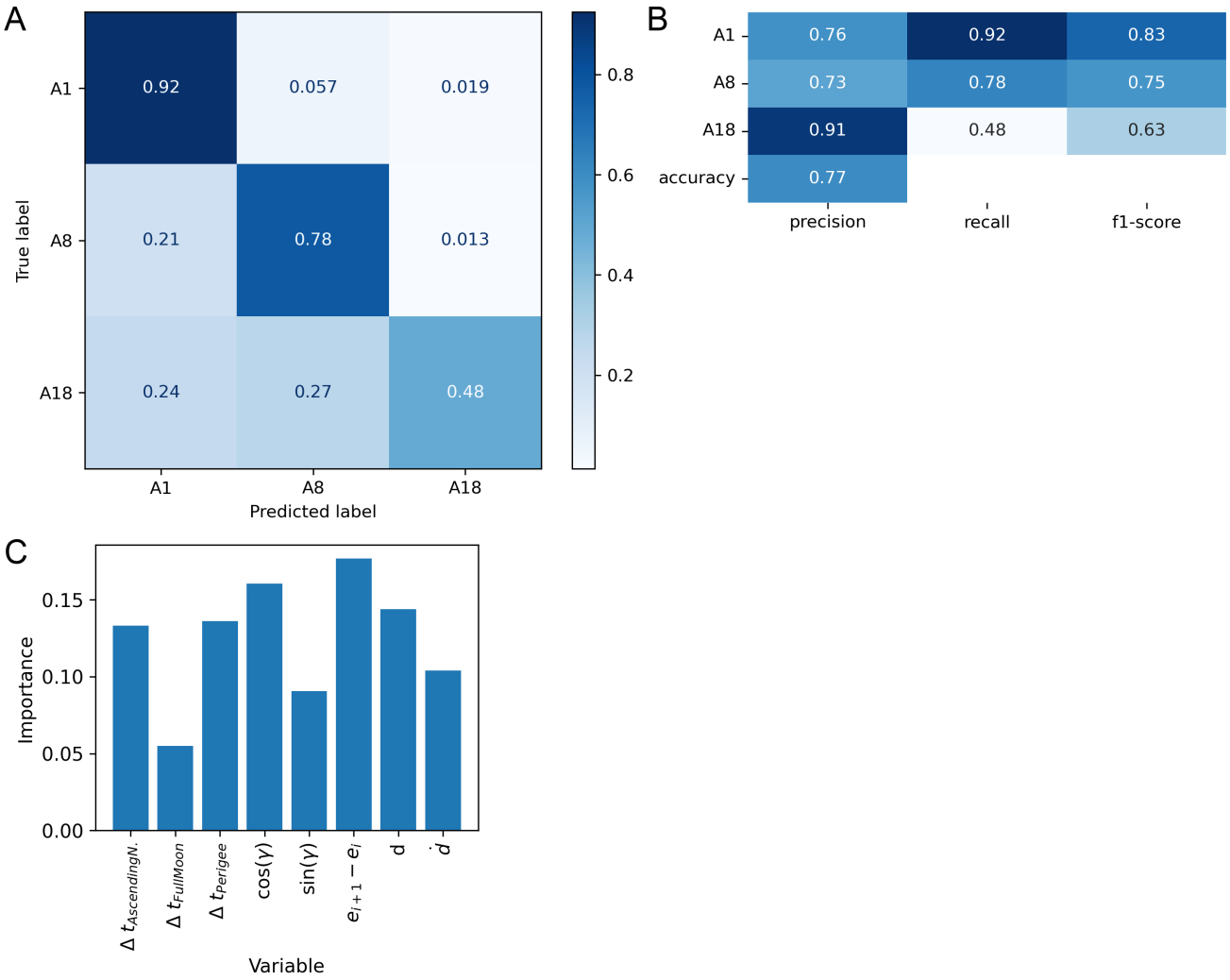

Figure S16. Same as Figure S6, but classifying three nests A1, A8 and A18.

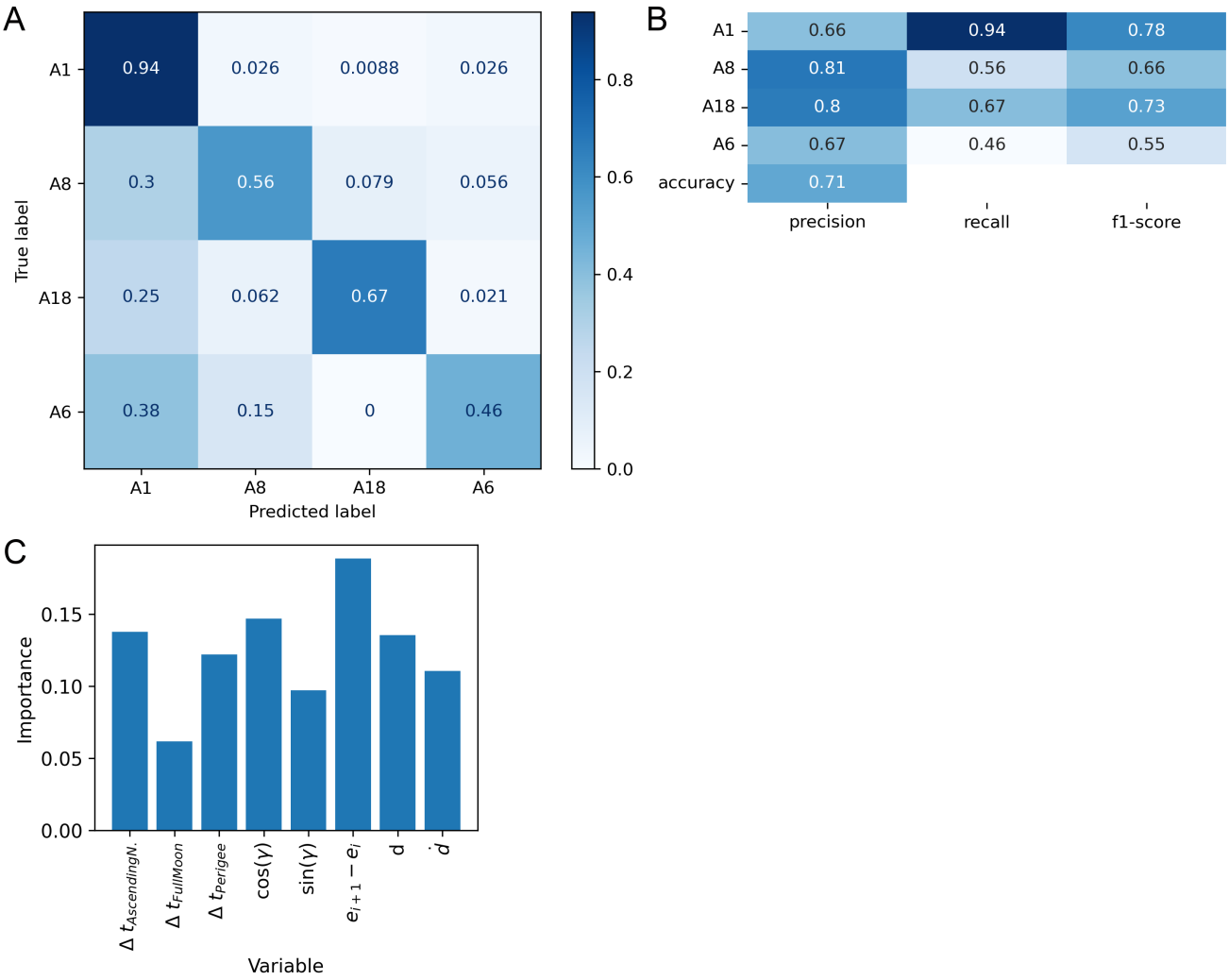

Figure S17. Same as Figure S6, but classifying four nests A1, A8, A18, A6.

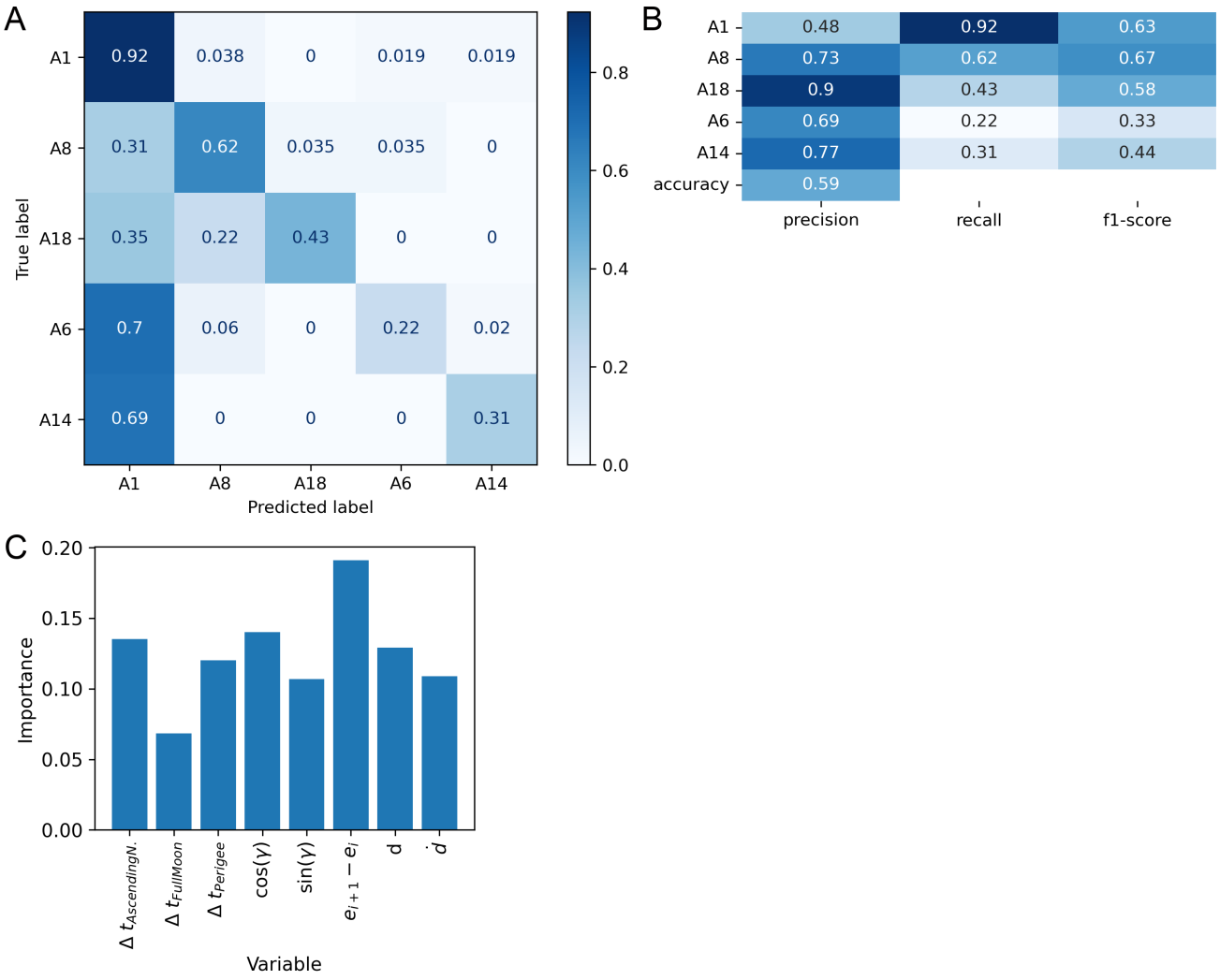

Figure S18. Same as Figure S6, but classifying five nests A1, A8, A18, A6, A14.

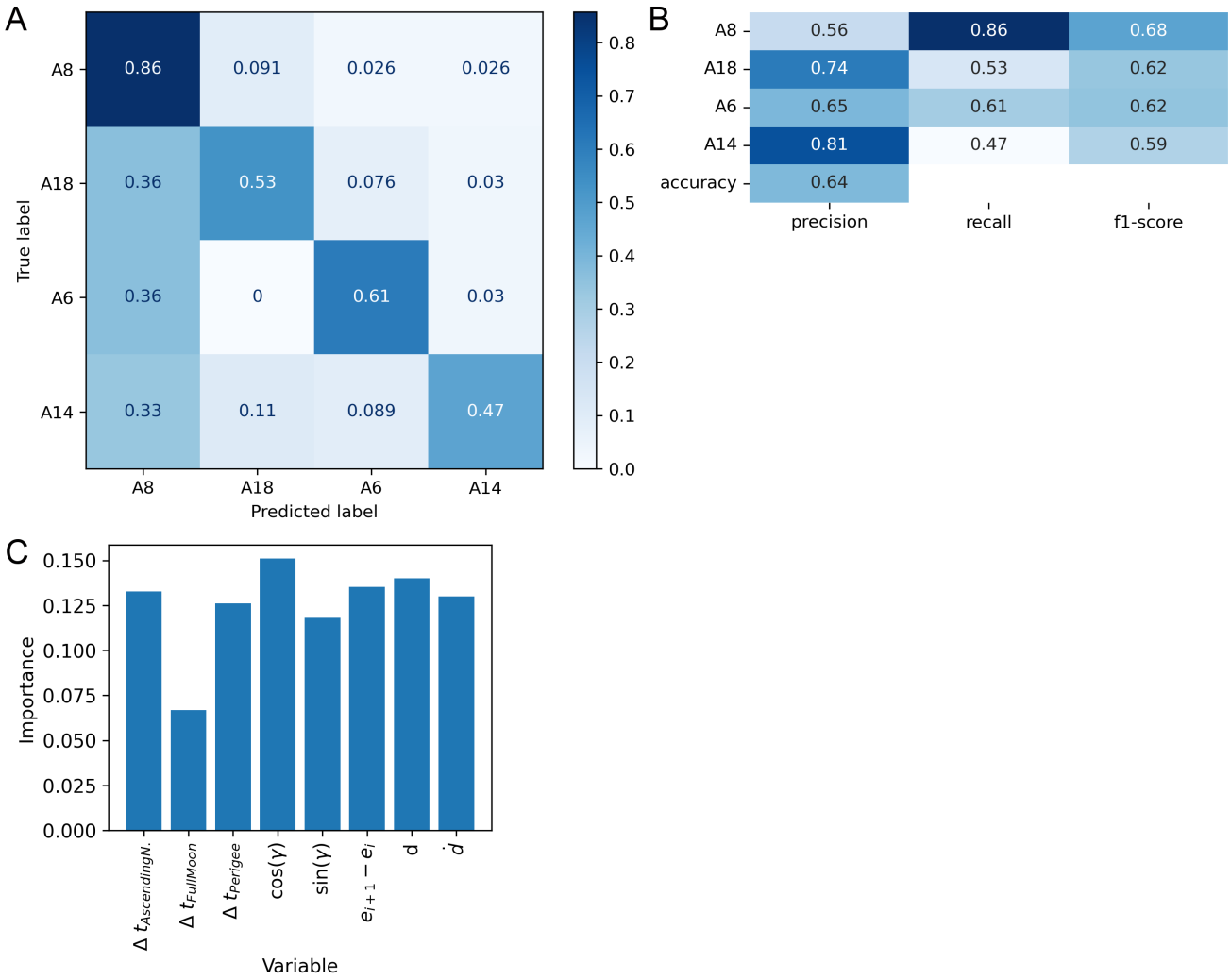

Figure S19. Same as Figure S6, but classifying four nests A8, A18, A6, A14.

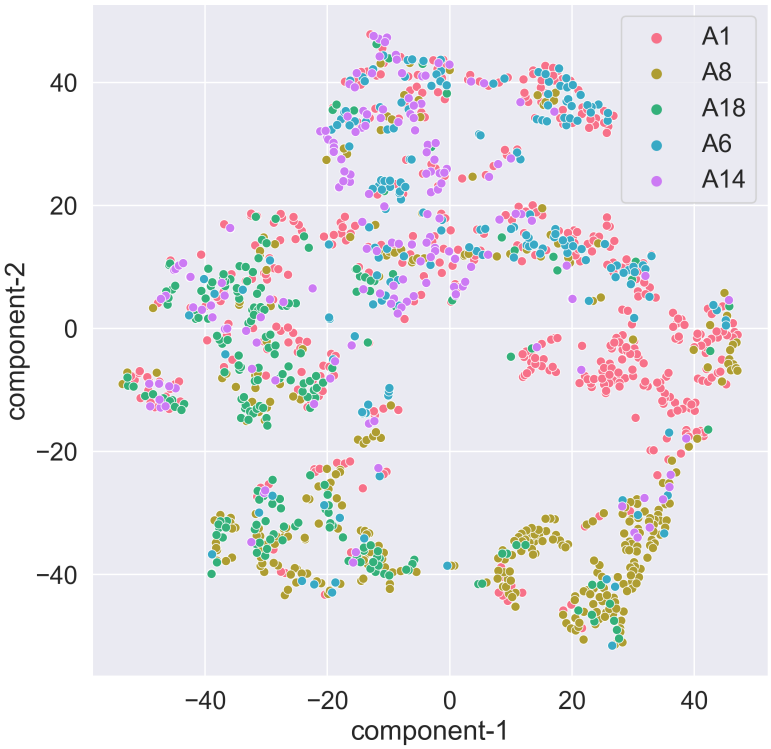

Figure S20. 2-D manifold of the feature space spanned by nests A1, A8, A18, A6, A14.

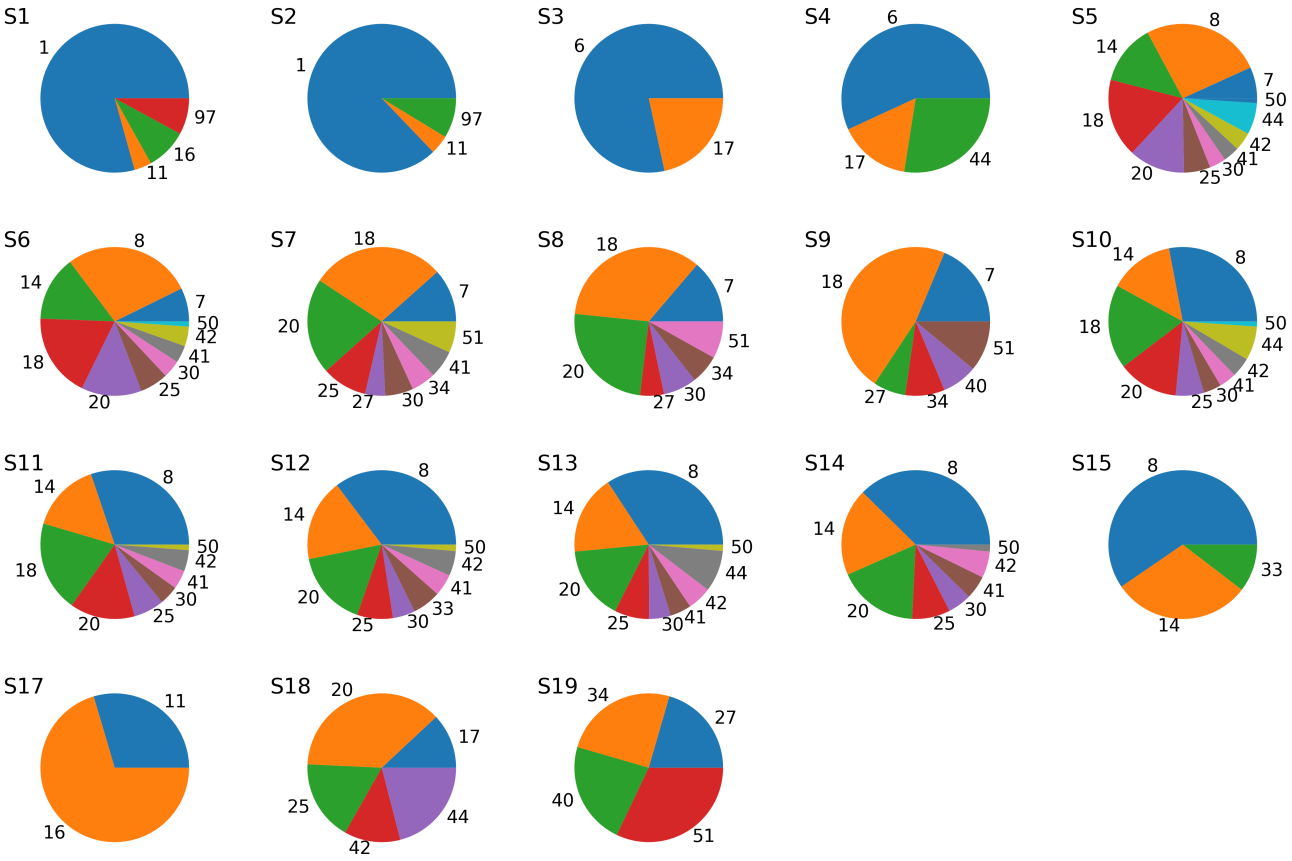

Figure S21. Pie charts for all sets shown in Figure 1 displaying the composition of the set and the contribution of each nest within the each set.

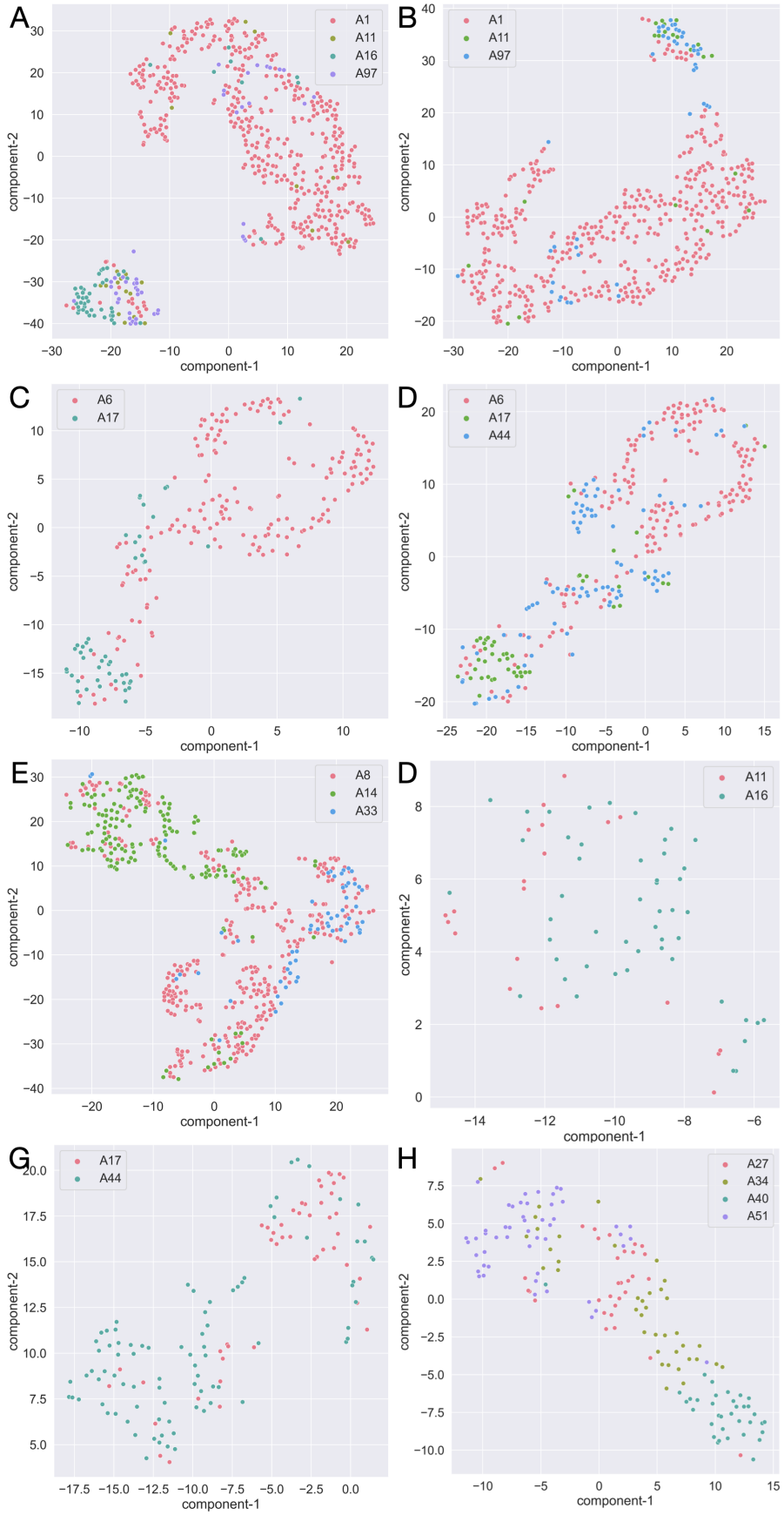

Figure S22. 2-D manifold of the feature space spanned by nests belonging to defined sets S_i: A) S1, B) S2, C) S3, D) S4, E) S12, F) S13, G) S14, H) S15.

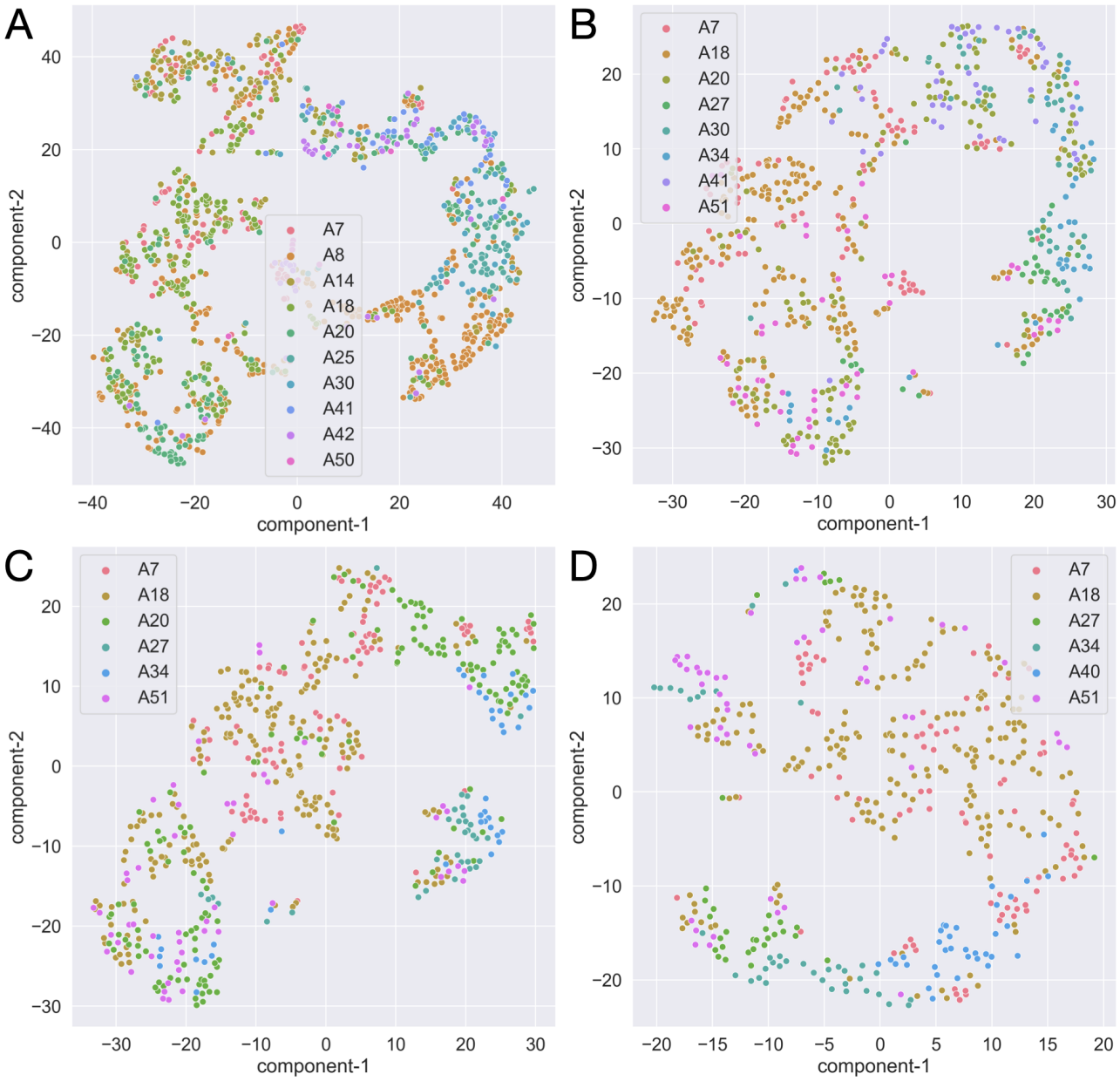

Figure S23. 2-D manifold of the feature space spanned by nests belonging to defined sets S_i: A) S5, B) S6, C) S7, D) S8

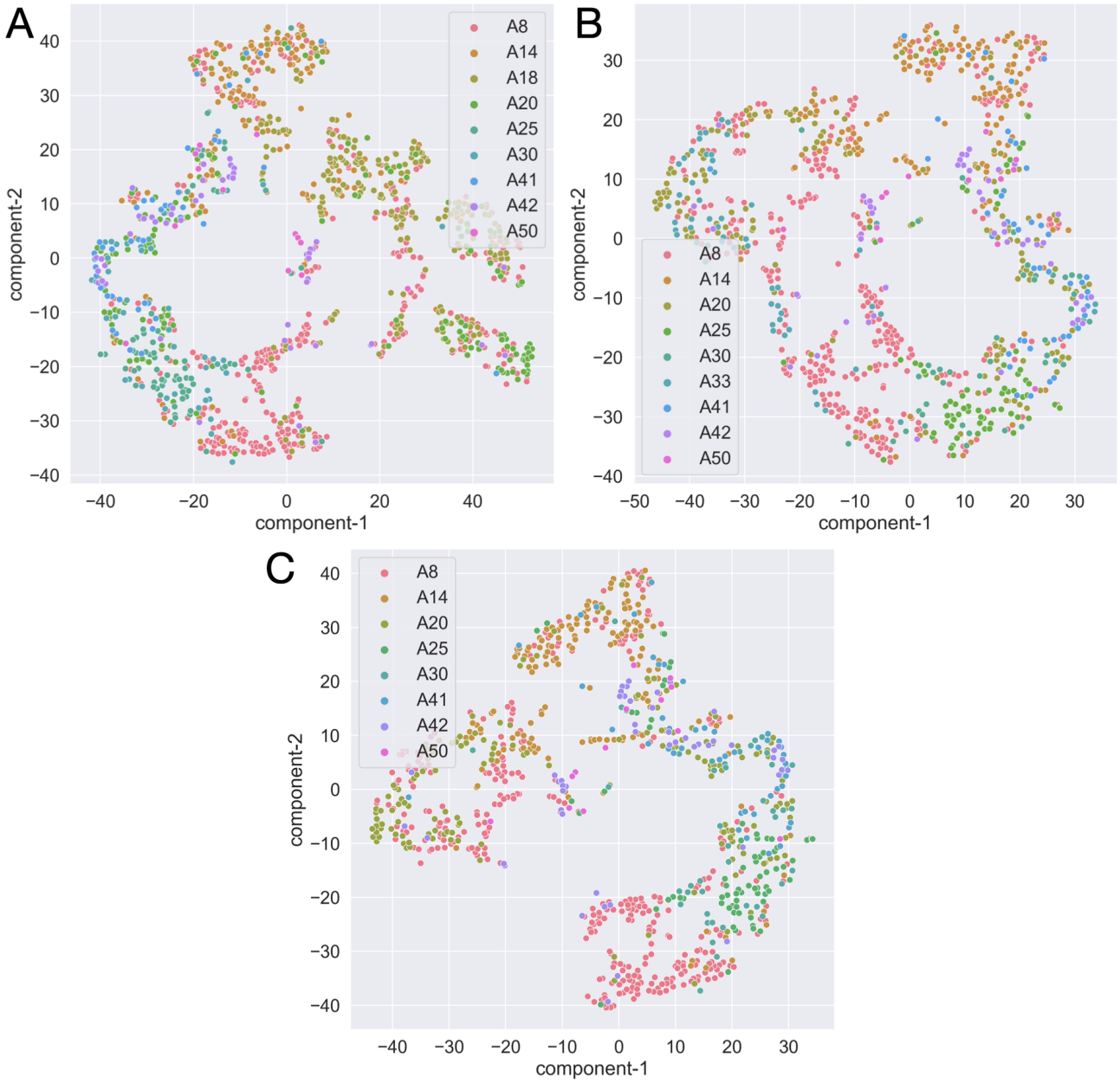

Figure S24. 2-D manifold of the feature space spanned by nests belonging to defined sets S_i: A) S9, B) S10, C) S11.